AD_____

GRANT NUMBER DAMD17-97-1-7118

TITLE: Few-View Tomographic Reconstruction of Technetium-99m-sestamibi Distribution for the Detection and Diagnosis of Breast Lesions

PRINCIPAL INVESTIGATOR: Patrick J. La Riviere

CONTRACTING ORGANIZATION: University of Chicago
Chicago, Illinois 60637

REPORT DATE: August 1998

TYPE OF REPORT: Annual

PREPARED FOR: Commanding General
U.S. Army Medical Research and Materiel Command
Fort Detrick, Maryland 21702-5400

DISTRIBUTION STATEMENT: Approved for Public Release;
Distribution Unlimited

REPORT DOCUMENTATION PAGE

Public reporting burden for this collection of information is estimated to average 1 hour per response, including the time for reviewing instructions, searching existing data sources, gathering and maintaining the data needed, and completing and reviewing the collection of information. Send comments regarding this burden estimate or any other aspect of this collection of information, including suggestions for reducing this burden, to Washington Headquarters Services, Directorate for Information Operations and Reports, 1215 Jefferson Davis Highway, Suite 1204, Arlington, VA 22202-4302, and to the Office of Management and Budget, Paperwork Reduction Project (0704-0188), Washington, DC 20503.

1. AGENCY USE ONLY *(Leave blank)*	2. REPORT DATE August 1998	3. REPORT TYPE AND DATES COVERED Annual (15 Jul 97 - 14 Jul 98)

4. TITLE AND SUBTITLE
Few-View Tomographic Reconstruction of Technetium-99m-sestamibi Distribution for the Detection and Diagnosis of Breast Lesions

5. FUNDING NUMBERS
DAMD17-97-1-7118

6. AUTHOR(S)
Patrick J. La Riviere

7. PERFORMING ORGANIZATION NAME(S) AND ADDRESS(ES)
University of Chicago
Chicago, Illinois 60637

8. PERFORMING ORGANIZATION REPORT NUMBER

9. SPONSORING / MONITORING AGENCY NAME(S) AND ADDRESS(ES)
U.S. Army Medical Research and Materiel Command
Fort Detrick, Maryland 21702-5400

10. SPONSORING / MONITORING AGENCY REPORT NUMBER

19990115 087

11. SUPPLEMENTARY NOTES

13. ABSTRACT *(Maximum 200 words)* Scintimammography (SMM) is a nuclear medicine test with the potential to provide relatively low-cost, minimally invasive differentiation of breast abnormalities detected by physical examination or mammography. While the most widely used clinical protocol involves acquiring one or two planar views, occasionally supplemented by conventional SPECT, we have used the ideal-observer SNR framework to establish that a dedicated breast SPECT geometry, in which the camera revolves around the breast alone, would provide superior lesion detectability to these other two approaches. Because the time required by tomographic studies to acquire data useful to popular reconstruction algorithms might be excessive for SPECT SMM, we have worked to develop reconstruction algorithms that can generate diagnostically useful SMM images from a smaller number of views than is usually used. In particular, we have developed a technique in which the few-view sinogram is first smoothed using an effectively two-dimensional, adaptive smoothing algorithm and additional views are then interpolated using periodic spline interpolation. The spline interpolation approach was chosen after extensive investigation of the accuracy and noise properties of various periodic interpolation approaches. We find that using this technique, meaningful images can be reconstructed from as few as 16 angular views.

14. SUBJECT TERMS
Breast Cancer, Scintimammography, Tomography, Dedicated breast SPECT, Few-View Reconstruction

15. NUMBER OF PAGES 45

16. PRICE CODE

17. SECURITY CLASSIFICATION OF REPORT Unclassified	18. SECURITY CLASSIFICATION OF THIS PAGE Unclassified	19. SECURITY CLASSIFICATION OF ABSTRACT Unclassified	20. LIMITATION OF ABSTRACT Unlimited

FOREWORD

Opinions, interpretations, conclusions and recommendations are those of the author and are not necessarily endorsed by the U.S. Army.

____ Where copyrighted material is quoted, permission has been obtained to use such material.

____ Where material from documents designated for limited distribution is quoted, permission has been obtained to use the material.

____ Citations of commercial organizations and trade names in this report do not constitute an official Department of Army endorsement or approval of the products or services of these organizations.
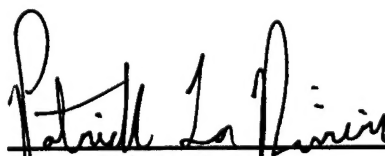
____ In conducting research using animals, the investigator(s) adhered to the "Guide for the Care and Use of Laboratory Animals," prepared by the Committee on Care and use of Laboratory Animals of the Institute of Laboratory Resources, national Research Council (NIH Publication No. 86-23, Revised 1985).

_✓_ For the protection of human subjects, the investigator(s) adhered to policies of applicable Federal Law 45 CFR 46.

____ In conducting research utilizing recombinant DNA technology, the investigator(s) adhered to current guidelines promulgated by the National Institutes of Health.

____ In the conduct of research utilizing recombinant DNA, the investigator(s) adhered to the NIH Guidelines for Research Involving Recombinant DNA Molecules.

____ In the conduct of research involving hazardous organisms, the investigator(s) adhered to the CDC-NIH Guide for Biosafety in Microbiological and Biomedical Laboratories.

PI - Signature   8/12/98
                                    Date

Contents

1

1 Introduction

1.1 Background

Breast cancer is the most frequently diagnosed invasive malignancy among American women and ranks second only to lung cancer in annual cancer-related mortality for this group [1]. Numerous studies have shown that early detection and treatment of breast cancer can improve survival rates [2–4]. Screen-film mammography has come to play a vital role in this detection process, due to its high (80-90%) sensitivity to breast malignancies. However, mammography is notoriously poor at distinguishing benign from malignant tumors, having reported specificities and positive predictive values of 15-30% [5]. This means that only a small percentage of lesions biopsied on the basis of suspicious mammographic appearance are found to be malignant.

In recent years, researchers have developed and studied a nuclear-medicine test with the potential to provide relatively low-cost, minimally invasive differentiation of breast abnormalities identified by physical examination or mammography [6–18]. Known as scintimammography (SMM), the test relies on the preferential uptake of Tc-99m-sestamibi or other radionuclides such as Tl-201, Tc-99m-tetrofosmin, or Tc-99m-MDP in breast malignancies as compared to normal breast tissue or benign abnormalities. Indeed, one study has shown that typical *in vivo* tumor-background concentration ratios of Tc-99m-sestamibi are 5.64 ± 3.06 [19]. This focal uptake can be imaged in a number of ways, though the most widely used clinical protocol involves acquiring one or two planar views—one lateral view and possibly an additional oblique or anterior view—while the patient lies prone on a specially designed table [20]. The imaging time is typically 10-15 minutes per view. Numerous clinical studies with histological follow-up have been performed using this or a similar protocol, reporting sensitivities of 83-96%, and specificities of 66-100% when using Tc-99m-sestamibi to image mammographically suspicious lesions [8–18]. In addition to differentiating breast abnormalities detected by other means, SMM may also have a role in the detection of breast malignancies in patients with radiographically dense breasts, for whom screen-film mammograms are often difficult to interpret [7].

A few of these studies of SMM have also examined the role of conventional single photon emission computed tomography (SPECT) (where the patient lies supine and the camera revolves around the torso) in detecting focal uptake of Tc-99m-sestamibi and have found comparable but not generally improved sensitivities as compared to planar techniques, along with substantially lower specificities [14, 21–23]. Wang *et al.* [24] speculated that this surprisingly poor performance was due to substantial attenuation of photons emitted in the breast by the torso in at least half of the views as well as to the presence of scatter from organs such as the heart and liver known to have high uptake of Tc-99m-sestamibi. The poor performance of conventional SPECT may also be related to the inferior resolution of conventional SPECT as compared to planar techniques in this situation, due to the fact that the scintillation cameras are on average further away from the breast in the conventional SPECT geometry than in the

2

planar geometry. Wang *et al.* also investigated a geometry that they called vertical axis-of-rotation SPECT and that we call dedicated breast SPECT, or simply dedicated SPECT, in which the scintillation cameras are assumed to revolve around one breast alone, with the patient lying prone. This geometry eliminates the effect of attenuation by the thorax and, with proper shielding, the effect of scatter from the thorax. Moreover, the small radius of rotation offers improved resolution and sensitivity. In phantom studies, Wang *et al.* found that with this dedicated geometry they were able to detect a breast lesion with an outer diameter of 1 cm and a 6:1 lesion-to-background concentration ratio that was not detectable in either conventional SPECT or planar studies with the same total imaging time.

While no one has yet developed a dedicated breast SPECT system for clinical use, encouraging results such as these make it an important and hopefully fruitful area of research. One practical concern that could limit the acceptance and use of dedicated SPECT SMM is the lengthy imaging time (on the order of 30–40 minutes) that would be required to acquire projection data useful to standard reconstruction algorithms such as filtered backprojection (FBP). Motion artifacts could be common as patients could find it difficult to remain still for this time while lying prone on an unpadded table (padding would interfere with imaging near the chest wall). Moreover, this lengthy imaging time would limit patient throughput, which is undesirable for a test that could potentially gain high-volume use as a follow-up to conventional mammography.

1.2   Purpose of research

The purpose of the research being undertaken is to reduce imaging time for dedicated SPECT scintimammography by developing algorithms tailored to generate diagnostically useful images from a smaller number of projection views than are usually used in emission tomography. The algorithms will take advantage of the simplicities and symmetries inherent in the SMM problem to extract a maximum of information from the views that *are* acquired, in contrast to reconstruction approaches such as the ever-popular filtered backprojection (FBP), which generally force the data to yield to their own implicit assumptions and lead to artifacts when they are not satisfied. For example, it is well known that FBP yields images with prominent star artifacts when the number of angular views is insufficient.

In the proposal, we proposed to investigate the use of a class of reconstruction approaches known as Algebraic Reconstruction Technique (ART) algorithms, which make no implicit assumptions about the completeness of the dataset but rather iteratively update the image in search of the solution that best agrees with the data (the precise definition of "best" allows for many variants of the basic ART algorithm). Specifically, the work of the first year was to have met three principal goals, as outlined in the proposal's Statement of Work:

1. To finish implementing the standard ART algorithm.

2. To systematically explore the dependence of reconstruction image quality on the number of projections and the complexity of the input image.

3. To modify the ART algorithm to perform a purely binary reconstruction of the tracer distribution.

1.3 Overview of research accomplishments

In practice, the year's research began by examining a more basic issue than that of optimizing reconstruction algorithms: the question of whether a dedicated SPECT geometry would indeed be better for SMM lesion detection than currently existing planar or conventional SPECT geometries. The experimental results of Wang *et al.* [24] mentioned above suggested that it would be, but we undertook to answer the question more definitively and quantitatively by using the so-called ideal-observer framework to quantify the amount of information contained in the projections of a breast phantom using the three different geometries. The results indicated conclusively that the dedicated SPECT geometry is superior. The same framework was then used to address goal 2—the determination of the dependence of reconstructed image quality on the number of projections acquired.

After firmly establishing the superiority of the dedicated SPECT geometry, we returned to the question of developing reconstruction algorithms tailored to few-view SMM data. Goal 1—implementation of the standard ART algorithm—was accomplished, though with disappointing results. Even in the absence of noise, the quality of the reconstructed images as compared to FBP was not sufficiently high to justify the large computational burden of the approach. In the presence of noise, images reconstructed by the ART approach were really quite poor, even compared to ramp-filtered FBP. These same general trends held for reconstructions from standard and small numbers of views, though the few-view FBP reconstructions were of course plagued by the star artifacts mentioned in Section 1.2. This poor performance of ART suggested that the exploration of binary ART reconstructions—goal 3—would not be fruitful, and that incorporation of the more explicitly statistical techniques and statistical priors planned for the second year's work would be more appropriate. In this vein, we have made an extensive search of the literature on statistical methods in image reconstruction, gathering and studying nearly 50 articles on the topic.

The surprisingly strong performance of FBP that came to light in the course of testing the ART approach, even in the face of a small number of projections, suggested that it might be fruitful to explore sinogram preprocessing approaches aimed at reducing the visual distraction of the star artifacts while preserving crucial image information. Put differently, we realized that the relative simplicity and symmetry of the object being imaged in dedicated SPECT SMM means that the number of angular views dictated by the Nyquist sampling condition is likely to be smaller than the number required to avoid the severe star artifacts common to few-view FBP reconstructions. In this situation, the additional views needed by FBP can in principal be interpolated from the measured ones.

4

This led to a detailed investigation of the properties of four popular interpolation approaches for periodic functions: linear interpolation (with periodic boundary conditions), periodic spline interpolation, circular sampling theorem interpolation, and zero-padding interpolation. The investigation consisted of three principal elements. First, we derived previously unappreciated equivalences among the methods, showing that zero-padding interpolation and circular sampling theorem interpolation are in some sense mathematically equivalent and that both are exact and equivalent to Whittaker-Shannon interpolation when interpolating a periodic, bandlimited function sampled in accordance wih the Nyquist sampling condition. Second, we performed an empirical study of the accuracy of the four methods in interpolating typical tomographic sinograms, finding periodic spline interpolation to be generally superior in this situation. Finally, we explored the noise properties of the four methods, deriving analytic expressions for the covariance of interpolated points given that the measured samples are corrupted by additive, zero-mean noise and we confirmed these findings with Monte Carlo studies.

Of course, interpolating among noisy data can be unwise, regardless of the noise properties of the interpolation method, so the next element of the year's work involved investigating the use of a novel, effectively two-dimensional, adaptive smoothing algorithm for smoothing the few-view sinogram prior to interpolation. The technique exploits Fourier transforms to reduce the dimensionality of the smoothing problem and then uses the popular penalized least-squares smoothing measure where the smoothing parameter is chosen automatically by GCV. We studied the use of the smoothing technique alone, on sinograms with a standard number of projections, and also in conjunction with interpolation for few-view sinograms.

Finally, because most of the sinogram preprocessing approaches described so far have involved fitting of continuous smoothing and interpolating splines to the measured data, we explored an alternative reconstruction approach to FBP that allows reconstruction to proceed directly from the coefficients of the splines fit at each projection angle. The approach was first proposed by Wahba [25], but we have simplified her approach, using relationships among spline coefficients to eliminate numerically unstable terms, and, perhaps most significantly, extended the approach to the three-dimensional Radon inversion problem, where it takes on a much simpler form than in two dimensions.

2 Body

2.1 Comparison of imaging geometries

2.1.1 Background

We examined quantitatively the question of lesion detectability in three different scintimammographic geometries—planar, conventional SPECT, and dedicated SPECT—using the so-called ideal-observer framework to calculate signal-to-noise ratios as a function of lesion concentration [26]. The ideal-observer frame-

work [27] offers a way of assessing the amount of information the data from an imaging device contain with regard to the performance of a specified task. For example, the simplest such task is the detection of a signal of known strength, shape, and location in a specified background. In this case, the framework seeks to quantify the degree to which an ideal observer—one who can use the information contained in the images to its fullest extent—can reliably distinguish images containing the background alone from images containing the background and the signal when both kinds of images are corrupted by noise, blurring, and other imperfections. For linear imaging processes in which the noise in the output image is assumed to be additive, Gaussian, zero-mean, stationary, and independent of the presence or absence of the signal, the ideal-observer framework allows us to characterize fully the quality of the imaging system data with respect to the performance of the specified signal-detection task by a single number, the ideal-observer signal-to-noise ratio (SNR). This is usually expressed as

$$SNR_I^2 = K^2 \int \frac{|\Delta S_{in}(v)|^2 \, MTF^2(v)}{W(v)} dv, \tag{1}$$

where K is the large-scale transfer characteristic of the imaging system at the desired operating point, $MTF(v)$ is the system modulation transfer function, $W(v)$ is the system Wiener spectrum, and $|\Delta S_{in}(v)|^2$ is the power spectrum of the signal in input space, i.e. before it has been scaled and degraded by the imaging system. This expression allows one to determine the ideal-observer SNR for *any* analytically specified input signal once K, $MTF(v)$, and $W(v)$ are known. Alternatively, if one wishes to determine the ideal-observer SNR for a particular real signal, equation (1) could be re-expressed as

$$SNR_I^2 = \int \frac{|\Delta S_{out}(v)|^2}{W(v)} dv, \tag{2}$$

where $|\Delta S_{out}(v)|^2$ is the power spectrum of the signal in output space, i.e. after it has been scaled and degraded by the imaging system.

The images whose information content we wish to measure are not reconstructed images but rather the raw projection images acquired by the various imaging systems, for these offer the purest measure of the quality of the data acquired by the imaging system. The process of image reconstruction, while certainly helpful to human observers, can never increase the ideal-observer SNR and generally reduces it. Using reconstructed images to compare imaging geometries would thus conflate issues of data quality with issues of reconstruction algorithm accuracy. (Of course, once the ideal-observer SNR of the projection data is known, ideal-observer analysis of reconstructed images can be used to evaluate which reconstruction algorithms best *preserve* the information content of the raw projections). Because the noise in the projection images is uncorrelated, equation (2) takes on a particularly simple form in this case,

$$SNR_I^2 = \Delta s^t (diag\left\{\langle p(\xi_i, \phi_j)\rangle\right\})^{-1} \Delta s, \tag{3}$$

6

where Δs is the signal vector, $diag\{\}$ represents a diagonal matrix and $\langle p(\xi_i, \phi_j)\rangle$ is the noise free projection of the background at projection bin ξ_i and projection angles ϕ_j [28].

2.1.2 Methods

As discussed above, computing the ideal-observer SNR for a given imaging geometry and processing approach requires two ensembles of projection images: one set consisting of images of the signal alone and one set consisting of images of the background alone. Our background consisted of an 14-cm diameter, 800 cc cylindrical phantom and our signal was a 1-cm outer diameter spherical lesion insert. This lesion size is representative of the smallest currently detected in scintimammography. For each geometry we acquired 20 images of the background alone, for which we put 3.7 mCi of activity in the phantom and imaged for 1 minute total for each conventional or dedicated SPECT acquisition and 30 seconds for each planar view. These combinations of activity and imaging time were chosen to produce clinically realistic count levels using the following reasoning. As with Wang *et al.*, we began with the assumption that 1% of a typical 25 mCi clinical dose of Tc-99m-sestamibi is taken up by the myocardium. Using the volume of the myocardium in the Data Spectrum Corporation cardiac insert as a guide, along with the assumption that soft tissue will have a 1:15 concentration relative to the myocardium allowed us to determine the expected concentration of activity in healthy breast tissue. We wished to compare detectability in these three geometries given the same total imaging time, and assumed that typical clinical imaging times would be 30 minutes per SPECT study and 15 minutes per planar view. Thus we were comparing the three geometries for equal total imaging times given that two-view planar studies are common. Given this, we scaled up the calculated concentration by a factor of 30 and scaled down the imaging times by the same factor to allow for more rapid data acquisition. All imaging times were adjusted to compensate for the decay of the activity. To image the lesion we filled it with 7.6 mCi of Tc-99m, placed it in the cylinder now filled with cold (zero-activity) water, and imaged for 30 minutes in conventional and dedicated SPECT and 20 minutes for the planar view. This combination of activity and imaging time was chosen simply to provide high-count, low noise images of the signal, as required by the theory.

The dedicated SPECT images were acquired by placing the phantom at the center of rotation of a Picker XP2000 two-headed SPECT system with the heads rotating at the minimum radius of rotation (9.0 cm). In this configuration the heads were within 2.0 cm of the walls of the phantom. The breast phantom was not attached to an anthropomorphic torso phantom because Wang *et al.* showed that with proper shielding the contribution of scatter from the torso can be made negligible. We acquired 120 views over 360° with each head acquiring to a 128x128 matrix (pixel size=4.67 mm). We used a low-energy, ultra-high resolution collimator. The conventional SPECT images were also acquired in the absence of an anthropomorphic torso phantom, although the radius of rotation (25 cm) and the placement of the breast phantom (17 cm off-center) were deter-

mined with the torso phantom in place. The reason for this curious arrangement was to isolate the effect of the large radius of rotation on lesion detectability, without the additional degradations caused by attenuation or scatter in the torso. The ideal-observer SNR results for this arrangement will thus represent an *upper bound* on the true detectability. In other respects, the conventional SPECT images used the same acquisition parameters as the dedicated SPECT. Finally, the planar view was acquired with the phantom flush against one head, which acquired on a 128x128 matrix with a magnification factor of 2.0 (pixel size=2.33 mm). The ideal-observer SNR for the planar view was calculated using equation (3) directly. For the tomographic studies, equation (3) was applied to the two-dimensional sinogram corrsponding to the slice through the center of the lesion.

2.1.3   Results and conclusions

The ideal-observer SNRs for the detection of a 1-cm lesion with a 6:1 lesion-background concentration ratio are listed in Table 1 for the three geometries. The SNR values given suggest that a dedicated SPECT geometry would lead to improved detectability for clinically typical lesions over the planar and conventional SPECT geometries, especially since in the presence of attenuation and scatter from the torso we would expect the difference between the dedicated and conventional SPECT geometries to be even greater than it is here. The success of the dedicated geometry can be attributed to the fact that it combines the advantages of the other two approaches: because of its small radius of rotation, it offers good sensitivity and resolution comparable to that of a planar view acquired with the scintillation camera flush against the phantom, while it offers the improved contrast offered by a tomographic system's ability to separate lesion activity from overlying and underlying activity.

Planar SNR	Conventional SPECT SNR	Dedicated SPECT SNR
6.2	6.7	10.7

Table 1: Ideal-observer SNRs for detection of a 6:1, 1-cm lesion using planar, conventional SPECT, and dedicated SPECT scintimammography.

Having used the ideal-observer SNR framework to confirm that a dedicated SPECT geometry should offer superior lesion detectability to the conventional SPECT or planar geometries, we used the same approach to address goal 2, the dependence of the dedicated SPECT projection data SNR on the number of input angles used. The result is illustrated in Fig. 1. The SNR is seen to increase approximately as the square root of the number of angles used, indicating a diminishing SNR return as the number of angles is augmented, and holding some promise for the potential of few-view imaging techniques.
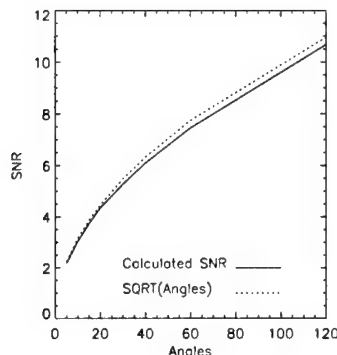
8

Figure 1: Dependence of sinogram ideal-observer SNR on the number of angular views used in imaging a 1-cm, 6:1 lesion with a dedicated SPECT geometry. For reference, the curve $\sqrt{\text{Angles}}$ is plotted as well.

2.2 Algebraic reconstruction techniques

2.2.1 Background

Having established the superiority of the dedicated SPECT geometry and the promising square-root dependence of SNR on the number of angles used, we began to concentrate on the development of algorithms capable of producing clinically useful images from a smaller number of angular views than is usually used. We focused first on the class of algorithms known as algebraic reconstruction techniques (ART), for unlike FBP these make no implicit assumptions about the completeness of the data but rather seek to produce iteratively a solution that best matches the data is available, according to some precise definition of "best."

In their most basic form, ART algorithms begin with an initial "guess" of the image, often just a uniform image, then project this estimate and compare to the measured data. The resulting differences are used to update the image pixel values. The process continues either for a prespecified number of iterations or until the magnitude of the changes from one iteration to the next falls below some prespecified threshold. One popular form of the iterative update procedure is given by the following equation

$$x^{(k+1)} = x^{(k)} + \frac{y_{i_k} - <r_{i_k}, x^{(k)}>}{<r_{i_k}, r_{i_k}>} r_{i_k}, \qquad (4)$$

where $x^{(k)}$ and $x^{(k+1)}$ represent the current estimate of the image vector after the kth and $(k+1)$st iterations, respectively, $i_k = [k(\text{mod}I) + 1]$, I is the total number of projection rays, y_{i_k} is the measurement for the i_kth projection ray, r_{i_k} is the transpose of the i_kth row of the projection matrix R relating the image vector to the measurement vector, and $\langle\rangle$ denotes an inner product [29, chapter 10].

9

2.2.2 Methods

In accordance with goal 1, mentioned in Section 1.2, we finished implementing an ART algorithm that made use of equation (4). The i, jth element of the projection matrix R was chosen to equal the intersection length between the ith pixel and the jth projection ray. To calculate these intersection lengths, we used an efficient algorithm, due to Siddon [30], in which the intersections of rays with separate grids of parallel horizontal and vertical lines are computed, the intersections ordered appropriately, and the differences computed. In the interest of storage efficiency, we stored the weights corresponding only to a single projection view at any one time, recomputing them anew at each iteration. To further reduce storage requirements, we only stored non-zero weight elements along with a separate list of their corresponding indices.

We tested the algorithm by reconstructing images of a numerical breast phantom containing large, low-contrast background structures, as well as two small lesions, one centrally and the other peripherally located. Because all of the structures are ellipses, the phantom's projections could be computed analytically, and we generated sinograms of 64 angles x 64 bins and 16 angles x 64 bins. We reconstructed each of these using ART and FBP (using a ramp filter with cutoff at the Nyquist frequency). We then added Poisson noise (200,000 total counts in the 64-angle sinogram, 50,000 counts in the 16-angle sinogram) and reconstructed using the same techniques.

2.2.3 Results and conclusions

The results of the ART and FBP reconstructions are illustrated in Fig. 2.
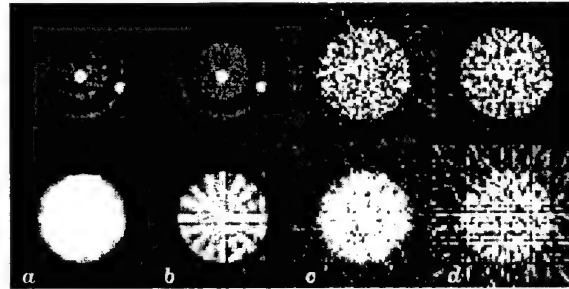
Figure 2: Reconstructions of a numerical breast phantom using ART and FBP. The top row corresponds to a 64-angle sinogram and and the bottom row to a 16-angle sinogram. Column (a) is reconstructed by ART from noise-free data, column (b) by FBP from noise-free data, column (c) by ART from noisy data, and column (d) by FBP from noisy data.

The ART reconstructions are obviously disappointing and especially so in the presence of noise. Both methods perform well for the noise-free reconstructions from 64 angles, but in the presence of noise, it is more difficult to discern

10

the lesions in the ART reconstruction than in the FBP image. Moreover, the ART reconstruction contains noise structures that could be mistaken for lesions. In the noise-free, 16-angle reconstructions, the lesions are again more visible in the FBP reconstruction despite the presence of distracting star artifacts. Finally, while the lesions are difficult to discern in either of the noisy 16-angle reconstructions, the FBP reconstruction again seems superior. Coupled with the fact that ART is much more computationally intensive than FBP, these results are quite disappointing.

The reasons for ART's poor performance in the noise-free case may lie in the combination of numerical instability and the lack of regularization in the straightforward ART implementation of equation (4). Clearly these factors are only exacerbated in the presence of noise. These poor results dissuaded us from pursuing goal 3, the design of a binary ART algorithm, until the performance of the basic iterative algorithm could be improved. The shortcomings of the ART reconstructions suggested looking into means of regularizing ART, which in turn pointed toward ways of incorporating explicit statistical information into the reconstruction process, a step that had been planned for year 2 of the grant. At present, we are conducting an extensive literature search, to gain exposure to and understanding of the very rich field of statistical image reconstruction.

2.3   Sinogram interpolation and interpolation method properties

2.3.1   Background

The surprising success of FBP in the comparisons with ART, even for few-view reconstructions, prompted us to reconsider its application to the few-view reconstruction problem. It is well-known that the principal drawback of few-view FBP reconstructions is the presence of a prominent star-shaped artifact in the background. This artifact can arise even when the angular sampling is in accordance with the Nyquist condition and is due to the fact that FBP, being based on a continuous, analytic Radon inversion formula, implicitly assumes the projection data is approximately continuous in the angular variable. If the data is only sparsely sampled in the angular variable, the negative side lobes introduced by the reconstruction filter fail to cancel in the intended way, giving rise to star-shaped artifacts. In principal, when the data satisfies the Nyquist condition at least approximately but fails to satisfy FBP's assumptions—a situation that can arise when the object being imaged is relatively simple or symmetric— additional views can simply be interpolated from the available ones and FBP used to reconstruct.

The interpolation method used should of course exploit the periodicity of the data in the angular coordinate, and we have explored four popular periodic interpolation approaches: linear interpolation with periodic boundary conditions, periodic spline interpolation, zero-padding (ZP) interpolation, and circular-sampling theorem interpolation (CST). Linear interpolation needs no introduction, and ZP is also quite familiar: it involves extending the discrete

Fourier transform (DFT) of a finite sequence with zeroes and then taking an inverse DFT to obtain a more densely sampled version of the sequence, with values interpolated at intermediate positions between the original measured samples [31–33]. CST interpolation is a special case of Whittaker-Shannon (W-S) sinc interpolation that applies to periodic functions. The CST holds that if a function $g(x)$ is periodic with period X, it can be reconstructed from a finite number N of samples taken over one period. Specifically, consider $g(x)$ to be sampled such that $g_n = g(n\Delta x)$, where $\Delta x = X/N$ and $n = 0, \ldots, N-1$. If $g(x)$ is bandlimited to frequency K (i.e., the coefficients of expansion a_k of the function's Fourier series satisfy $a_k = 0$ for $|k| > K$), and if $N \geq 2K + 1$ and is odd, then $g(x)$ can be reconstructed exactly from its samples by use of

$$g(x) = \sum_{n=0}^{N-1} g_n \frac{\sin\left[\frac{\pi}{\Delta x}(x - n\Delta x)\right]}{N \sin\left[\frac{\pi}{X}(x - n\Delta x)\right]}. \tag{5}$$

Similarly, if $N \geq 2K$ and is even, then the value of $g(x)$ may be determined exactly at arbitrary x using

$$g(x) = \sum_{n=0}^{N-1} g_n \left\{ \frac{\sin\left[\frac{\pi}{X}(N-1)(x - n\Delta x)\right]}{N \sin\left[\frac{\pi}{X}(x - n\Delta x)\right]} + \frac{1}{N}\cos\left[\frac{\pi}{\Delta x}(x - n\Delta x)\right] \right\}. \tag{6}$$

As for periodic spline interpolation, it involves fitting the data with pieceiwse cubic polynomials that are continuous up to and including the second derivative at the joints between pieces [34,35]. A spline $g(x)$ can be represented by

$$g(x) = a_n + b_n(x - x_n) + c_n(x - x_n)^2 + d_n(x - x_n)^3, \quad x \in [x_n, x_{n+1}], \tag{7}$$

and it can be shown that the coefficients a_n, b_n, c_n, and d_n can be obtained from the vector $\mathbf{g}$ of measured data points through matrix multiplications of the form $\mathbf{a} = \mathbf{A}\mathbf{g}$, where the matrices such as $\mathbf{A}$ are independent of the data and are constructed in accordance with periodic boundary conditions.

The first aspect of the interpolation work was to explore the little-understood connections among ZP, CST, and W-S interpolation. We showed that they are in fact mathematically equivalent for the task of increasing the density of angular samples, with zero-padding being considerably more computationally efficient, so we could omit CST from the list of approaches being considered for sinogram interpolation. Next we used statistical hypothesis testing to examine the empirical accuracy of the interpolation methods for the task of interpolating additional sinogram views. Finally, we examined the noise properties of the various interpolation methods, deriving expressions for the variance and covariance at points in interpolated functions given that the measured points are corrupted by either white or Poisson noise.

12

2.3.2 Methods

Connection between zero-padding, CST, and W-S interpolation

The connection between zero-padding, CST, and W-S interpolation was derived
using both a graphical and a mathematical approach [36]; the derivations are
different for the cases when the number of initial samples N is even or odd.
In the interest of space, we summarize here only the graphical proof for the
case when N is odd. Consider an arbitrary complex function $g(x)$, which is
not necessarily periodic, bandlimited, or compact, and which has a Fourier
transform $G(f)$. The real parts of these functions are illustrated in Fig. 3(a).
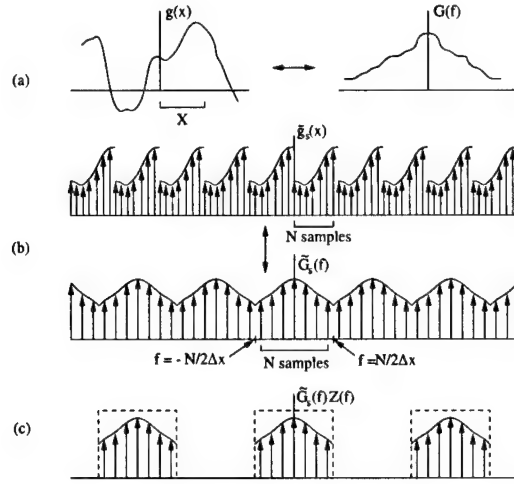

Figure 3: (a) The real parts of an arbitrary function $g(x)$ and its Fourier trans-
form $G(f)$. Also shown is the subinterval X that will be sampled. (b) The DFT
pair samples are implicitly samples of periodic functions in both the spatial and
frequency domains. The continuous spatial-domain function $\widetilde{g}(x)$ is the periodic
extension of the subinterval X, while the frequency-domain function $\widetilde{G}(f)$ arises
from aliased replications of the original Fourier transform further modified as
a result of the truncation of $g(x)$. Shown are the sampled versions of $\widetilde{g}(x)$ and
$\widetilde{G}(f)$, denoted $\widetilde{g}_s(x)$ and $\widetilde{G}_s(f)$, respectively. The principal periods of N sam-
ples in each space (which correspond to the N values of the DFT pair) are also
indicated. (c) The operation of zero-padding the DFT samples is equivalent to
multiplying by a sequence of rect functions, as shown.

The function is sampled N times (where N is an odd number) over a sub-interval
of length X, with sampling distance $\Delta x = X/N$ (without loss of generality, we
assume that the first sample lies at $x = 0$). In order to appreciate the effects
of zero-padding the DFT of this sequence, it is necessary to understand the
relationship of the DFT pair to the true function $g(x)$ and the true spectrum
$G(f)$. The DFT pair consists of the N space-domain samples of $g(x)$ and the

13

N corresponding frequency-domain samples yielded by the DFT. Implicitly, however, each sequence represents samples of a single period of a continuous periodic function [37]. In the spatial domain, this function, which we call $\widetilde{g}(x)$, is simply the periodic extension of the subinterval of $g(x)$ that we have sampled; that is, $\widetilde{g}(x)$ is the periodic function that arises when this subinterval of length X is replicated every X units. In the frequency domain, we have a function that we call $\widetilde{G}(f)$, which is periodic with period $1/\Delta x$. It is composed of aliases of the true spectrum and is generally also degraded by oscillations introduced in truncating $g(x)$. The sampled functions, which we denote $\widetilde{g}_s(x)$ and $\widetilde{G}_s(f)$, are illustrated in Fig. 3(b) and can be represented mathematically as $\widetilde{g}_s(x) = \widetilde{g}(x) \sum_{n=-\infty}^{\infty} \delta(x - n\Delta x)$ and $\widetilde{G}_s(f) = \widetilde{G}(f) \sum_{m=-\infty}^{\infty} \delta(f - m/N\Delta x)$.

Appreciating the implicit periodicity of the DFT pair is important in understanding the space-domain effect of zero-padding in frequency space because any modification to the single period of samples available affects all the other periods as well. With this in mind, it is easy to see the zero-padding operation of extending the N available frequency-space samples with zeroes to PN samples (where P is an integer) is equivalent to multiplying the sampled periodic sequence $\widetilde{G}_s(f)$ by a periodic sequence of rect functions, as illustrated in Fig. 3(c) ($P = 2$ in this illustration). This sequence of rects, which we call $Z(f)$, can be represented mathematically as

$$Z(f) = \text{rect}(f\Delta x) * \sum_{l=-\infty}^{\infty} \delta\left(f - l\frac{P}{\Delta x}\right), \tag{8}$$

where $*$ denotes the operation of convolution and where

$$\text{rect}(f\Delta x) = \left\{ \begin{array}{ccc} 1 & |f\Delta x| < & 1/2 \\ 1/2 & |f\Delta x| = & 1/2 \\ 0 & |f\Delta x| > & 1/2. \end{array} \right. \tag{9}$$

Thus we have a new frequency-domain function $G'(f) = \widetilde{G}_s(f)Z(f)$, and by the convolution-multiplication theorem, the corresponding new spatial-domain function $g'(x)$ is given by $g'(x) = \widetilde{g}_s(x) * z(x)$, where $z(x)$ is the inverse Fourier transform of $Z(f)$ and we have used the fact that $\widetilde{g}_s(x)$ is the inverse Fourier transform of $\widetilde{G}_s(f)$. Of course, $z(x)$ can be determined from $Z(f)$ by another application of the convolution-multiplication theorem, using the fact that the Fourier transform of a rect is a sinc function and that the Fourier transform of a sequence of delta functions is itself a sequence of delta functions. Thus,

$$g'(x) = \left[\widetilde{g}(x) \sum_{n=-\infty}^{\infty} \delta(x - n\Delta x) \right] * \left[\text{sinc}(x/\Delta x) \sum_{l=-\infty}^{\infty} \delta\left(x - l\frac{\Delta x}{P}\right) \right]. \tag{10}$$

It can be shown that this expression is equivalent to:

$$g'(x) = \left\{ \sum_{n=-\infty}^{\infty} \widetilde{g}(n\Delta x)\text{sinc}\left[(x - n\Delta x)/\Delta x\right] \right\} \sum_{l=-\infty}^{\infty} \delta\left(x - l\frac{\Delta x}{P}\right), \tag{11}$$

which indicates that zero-padding the DFT of the Δx-spaced samples of $g(x)$ with ZP factor P is equivalent to convolving the samples of $\widetilde{g}(x)$ with a sinc function and then resampling the resulting curve with spacing $\Delta x/P$.

The periodicity of $\widetilde{g}(x)$ makes it possible to collapse the infinite sum in square brackets to a sum over a single period of $\widetilde{g}(x)$ using an identity that lies at the core of the CST. Specifically,

$$\sum_{n=-\infty}^{\infty} \widetilde{g}(n\Delta x)\mathrm{sinc}\left[(x-n\Delta x)/\Delta x\right] = \sum_{n=0}^{N-1} \widetilde{g}(n\Delta x)\frac{\sin\left[\frac{\pi}{\Delta x}\left(x-n\Delta x\right)\right]}{N\sin\left[\frac{\pi}{X}\left(x-n\Delta x\right)\right]}, \quad (12)$$

which allows us to write equation (11) as

$$g'(x) = \left\{\sum_{n=0}^{N-1} \widetilde{g}(n\Delta x)\frac{\sin\left[\frac{\pi}{\Delta x}\left(x-n\Delta x\right)\right]}{N\sin\left[\frac{\pi}{X}\left(x-n\Delta x\right)\right]}\right\} \sum_{l=-\infty}^{\infty} \delta\left(x-l\frac{\Delta x}{P}\right). \quad (13)$$

The proof of equation (12) is given by Stark [38] in the context of his derivation of the CST (the ratio of sine functions in equation (12) *is* the CST interpolation kernel), and while the functions in that work are assumed to be periodic and bandlimited, the proof of the above identity requires only the assumption of periodicity. The bandlimited constraint enters only in the claim that the sinc interpolation on the left-hand side of equation (12) is exact, a claim we do not yet make. At this point, equations (11) and (13) simply allow us to claim that *using zero-padding with zero-padding factor P to interpolate from an odd number N of Δx-spaced samples of an arbitrary function $g(x)$ is equivalent to applying the CST interpolation formula to those samples and resampling the resulting curve with spacing $\Delta x/P$ and is also equivalent to applying the W-S interpolation formula to the periodic extension of those samples and resampling that resulting curve with spacing $\Delta x/P$.* Cavicchi [39] derived a result similar to equation (13) without explicitly making the connection to the CST. Of course, a practical implementation of zero-padding only yields the NP samples lying between 0 and X. If $g(x)$ is actually periodic with period equal to the length of the sampled subinterval, X, then $\widetilde{g}(x) = g(x)$, and if $g(x)$ is also bandlimited to the Nyquist frequency $1/2\Delta x$, then the applications of the W-S and CST formulas in equations (11) and (13) are exact, and the expression in brackets in each of those equations is simply equal to $g(x)$. Under these conditions, then, both equations imply

$$g'(x) = g(x) \sum_{l=-\infty}^{\infty} \delta\left(x-l\frac{\Delta x}{P}\right). \quad (14)$$

That is, under these conditions, zero-padding returns exact values of $g(x)$ spaced by $\Delta x/P$. An essentially identical result was derived for the case when N is even.

Emprical accuracy studies

Having established this connection between zero-padding and CST interpolation, and their exactness for periodic, bandlimited data, we then examined their accuracy as well as the accuracy of periodic spline and linear interpolation in the face of typical, noise-free tomographic data. While theoretical arguments can be made about the strengths and weaknesses of these interpolation approaches, the arguments generally rely on assumptions that may not hold exactly for typical tomographic data. In view of this, we designed an empirical comparison in which we generated 100 different sinograms corresponding to a family of numerical breast phantoms. The 100 representatives of the family were generated by assigning a probability distribution to the parameters specifying the ellipses that made up the phantom, thus resulting in a varied but still recognizable set of phantoms. Noise-free sinograms of 512 angles by 64 bins were generated using the analytical expressions for the Radon transform of an ellipse. Each of these sinograms was subsampled at 16, 32, 64, 128, and 256 angles and then each of the three interpolation approaches was used to interpolate back to 512 angles. The normalized root-mean-square error (NRMSE) between the original and interpolated sinograms was computed. Each of the interpolated sinograms was then reconstructed using FBP and the NRMSE between the reconstruction and the numerical phantom was computed as well. Finally, paired t-tests and nonparametric signed rank tests were used to assess the significance of any difference in the performance of the three interpolation approaches from each of the numbers of starting samples.

Noise properties

In practice, of course, the samples of the functions of interest are invariably contaminated by noise, and it would be valuable to know how the noise corrupting the measured samples is propagated into the interpolated samples. Consider a periodic function $g(x)$ having period X that is sampled N times over one period, i.e. at points $x_n = Xn/N$ for $n = 0, \ldots, N-1$. Assume each measurement is corrupted by additive, zero-mean noise. The measured samples of $g(x)$ can then be represented as

$$\mathbf{g}(x_n) = \langle \mathbf{g}(x_n) \rangle + \mathbf{n}(x_n), \tag{15}$$

where bold-faced type denotes a random variable, $\langle \rangle$ represents the expectation operator and $\mathbf{g}(x_n)$ is the additive, zero-mean noise. Let $\widehat{\mathbf{g}}(x)$ be the curve interpolated from the noisy samples of equation (15). We compute the covariance of this function for two points x and x' by use of

$$\text{cov}(x, x') = \langle [\widehat{\mathbf{g}}(x) - \langle \widehat{\mathbf{g}}(x) \rangle] [\widehat{\mathbf{g}}(x') - \langle \widehat{\mathbf{g}}(x') \rangle] \rangle. \tag{16}$$

Of course, once the covariance has been computed, the variance at any point x is given by $\text{var}(x) = \text{cov}(x, x)$. Evaluation of equation (16) is straightforward for CST and ZP interpolation, but more subtle for spline interpolation. For the first two, $\widehat{\mathbf{g}}(x)$ has a relatively simple form, given by

16

$$\widehat{\mathbf{g}}(x) = \sum_{n=0}^{N-1} \mathbf{g}(x_n)\sigma_N(x - x_n), \tag{17}$$

where

$$\sigma_N(\theta) = \begin{cases} \sin(N\theta/2)/N\sin(\theta/2) & N \text{ odd} \\ \sin[(N-1)\theta/2]/N\sin(\theta/2) & N \text{ even.} \end{cases} \tag{18}$$

However, for periodic splines, as we see in equation (7), the function specifying $\widehat{\mathbf{g}}(x)$ for a particular x depends on the interval in which x falls. This can be handled by defining a vector of functions, indexed by the intervals between measured samples and realizing that equation (16) will yield a matrix of covariance functions, with each element corresponding to a pair of the intervals that x and x' can fall into. For the empirical studies we calculated analytically 128 (and 127) samples of a typical periodic function encountered in tomography: the angular function corresponding to one bin of the projection of a Shepp-Logan head phantom. We generated 50,000 noise realizations of these samples contaminated with additive, zero-mean Gaussian noise and 50,000 others with Poisson noise. We then interpolated each of these realizations to 1024 (and 1016) samples using the 3 methods discussed above. We calculated the empirical variance at each point as well as the empirical covariance between each of 9 samples and the remaining samples.

2.3.3 Results and conclusions

The results of the empirical accuracy study can be summarized as follows. In examining the sinogram NRMSE results, the following ranking held for both phantoms and for virtually every number of starting angles: periodic spline interpolation was superior to linear interpolation, which in turn was superior to zero-padding interpolation. The same general trends held for the reconstructed image NRMSE results, although the NRMSE tended to change very little for starting numbers of angles 128 or more, the errors due to angular sampling and interpolation effects having become small in comparison to the baseline errors of the reconstruction process itself. The relatively poor performance of zero-padding interpolation comes as a surprise, especially given the result, reported above, that zero-padding is exact and equivalent to Whittaker-Shannon interpolation when applied to periodic, bandlimited data. While tomographic data has been shown to be at least quasi-bandlimited in the angular direction, they are not exactly bandlimited, and zero-padding is apparently quite sensitive to departures from that assumption. Indeed, on inspecting typical zero-padding results, we saw that it lead to ringing artifacts near edges, the familiar Gibbs phenomenon. This ringing, which extends to either side of any such edge, results in a relatively large NRMSE compared to linear and spline interpolation, which react more locally. In conclusion, then, we find that periodic spline interpolation would be a wise choice for the interpolation of additional angular views for

noise-free or low noise data. It obviously leads to smoother, more flexible interpolating curves than linear interpolation with fewer of the non-local responses to violations of its assumptions that plague zero-padding.

As for the noise studies, we derived that the covariance of CST and ZP interpolated functions is

$$\text{cov}(x, x') = \sum_{j=0}^{N-1} \sum_{k=0}^{N-1} \sigma_N(x - x_j)\sigma_N(x - x_k) \langle \mathbf{n}(x_j)\mathbf{n}(x_k)\rangle. \qquad (19)$$

When the noise is white (i.e. $\langle \mathbf{n}(x_j)\mathbf{n}(x_k)\rangle = \sigma_o^2 \delta_{jk}$), one can show that $\text{cov}(x, x') = \sigma_o^2 \sigma_N(x - x')$. This has the interesting consequence for the variance that

$$\text{var}(x) = \begin{cases} \sigma_o^2 & N \text{ odd} \\ \sigma_o^2 \left(\frac{N-1}{N}\right) & N \text{ even.} \end{cases} \qquad (20)$$

We note two interesting facts about this result. First, the variance is constant at all points in the interpolated function, including points corresponding to the original measured points. Second, in the case when N is even, the variance is actually reduced relative to the variance in the measured data as well as to the variance in functions interpolated from an odd number of points. This argues for acquiring an even number of samples when performing this kind of interpolation, though the difference is small as N grows large. The variance result for N even is shown in Fig. 4(b).

For Poisson noise (i.e. $\langle \mathbf{n}(x_j)\mathbf{n}(x_k)\rangle = \langle \mathbf{p}(x_j)\rangle \delta_{jk}$), one can show that for slowly varying functions $\text{cov}(x, x') \cong \langle \mathbf{g}(x)\rangle \sigma_N(x - x')$ and thus that the variance is

$$\text{var}(x) = \begin{cases} \langle \mathbf{g}(x)\rangle & N \text{ odd} \\ \langle \mathbf{g}(x)\rangle \left(\frac{N-1}{N}\right) & N \text{ even.} \end{cases}$$

Again, the variance remains essentially unchanged from that found in the samples except for the slight, uniform reduction when N is even. The variance result for N even is shown in Fig. 4(e).

The analytic expression for the spline is unwieldy as it involves a sum of many products of the matrices like $\mathbf{A}$. As the resulting expression must be evaluated numerically to discern the form of the covariance and variance curves, we simply present the result of this evaluation for the variance for N even and Gaussian noise in Fig. 4(d), along with empirical variance results for both Gaussian and Poisson noise in Figs. 4(c) and 4(f). We observe here that the spline interpolation yields reduced variance between the measured samples, with the minimum located midway between samples while the original sample points themselves have unchanged variance. N being odd or even has no effect on the result.

Overall, then, we see that spline interpolation, in addition to its good accuracy also has desirable variance reduction properties. We also observe that when employing CST or ZP interpolation, using an even number of samples offers a slight reduction in variance at no cost in accuracy.
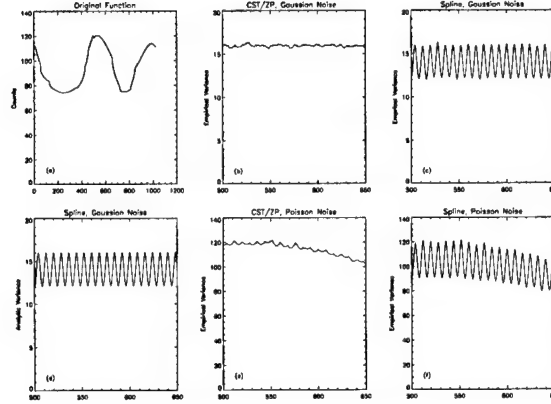
18

Figure 4: (a) Original function used in the interpolation studies. All the results shown here involved interpolating from 128 to 1024 samples of this analytically specified function. To emphasize detail, we show the variance only for a subinterval of the function. (b) Empirical variance for CST and ZP interpolation for Gaussian noise ($\sigma = 4$). This curve matches the analytic prediction of a constant variance equal to 15.875. (c) Empirical variance for periodic spline interpolation for Gaussian noise ($\sigma = 4$). The maxima correspond to points that coincide with the measured samples. (d) Analytically predicted variance for periodic spline interpolation for Gaussian noise ($\sigma = 4$). (e) Empirical variance for CST and ZP interpolation for Poisson noise. The variance, while locally flat is seen to track the variance of the original measured samples. (f) Empirical variance for periodic spline interpolation for Poisson noise. The variance behaves locally as in (c) but globally is seen to track the variance of the measured samples.

2.4 FBP with sinogram preprocessing and effectively 2D smoothing

2.4.1 Background

Despite the mild variance reduction offered by periodic spline interpolation, interpolating among noisy data is still a risky proposal. In principle, it would be desirable to smooth the data prior to interpolation. Ideally, we would like to perform a fully 2D, adaptive smoothing of the sinogram, as this would make maximal use of the correlations inherent in the data. Adaptive means that the degree of smoothing applied to various subsets of the data is determined automatically from the statistics in each subset separately, in contrast to a global smoothing operation that applies the same degree of smoothing to the entire data set. However, truly 2D adaptive smoothing algorithms are in general computationally expensive and difficult to implement [40]. In response, we have developed a method for achieving efficient, effective 2D adaptive smoothing by exploiting Fourier transforms to reduce the smoothing problem to a 1D one.

2.4.2 Methods

Consider a 2D discrete sinogram $p(\xi_i, \theta_j)$, where ξ_i refers to the ith projection bin $(i = 1, \ldots, N)$ and θ_j the jth projection angle $(j = 1, \ldots, M)$. It can be shown [41] that the following sequence of operations is equivalent to an adaptive, 2D smoothing of the sinogram:

1. Take a 1D discrete Fourier transform of the sinogram with respect to the projection angle θ_j; the result can be viewed as a set of 1D functions of the untransformed variable ξ_i, each labeled by an angular frequency index k, i.e. $P_k(\xi_i)$.

2. Perform an adaptive 1D smoothing of each of these M functions of ξ_i, yielding M discrete smoothed functions $P_k^s(\xi_i)$, where the superscript s stands for smoothed.

3. Perform an inverse 1D discrete Fourier transform of $P_k^s(\xi_i)$ with respect to the angular frequency k to recover $p^s(\xi_i, \theta_j)$.

The adaptive 1D smoothing we perform on each of the M functions $P_k(\xi_i)$ is known as penalized least-squares smoothing [27,28], and involves fitting the discrete data with a continuous smoothing curve $P_k^s(\xi)$ that minimizes the functional

$$S\{P_k^s(\xi)\} = \sum_{i=1}^{N} [P_k(\xi_i) - P_k^s(\xi_i)]^2 + \alpha \int_0^T [(P_k^s(\xi))'']^2 d\xi, \tag{21}$$

where ξ is a continuous variable representing the position along a given projection, T is the total length of the projection, and the double prime denotes the second derivative with respect to ξ. The two terms in this functional represent the competing goals of achieving a good fit to the data while maintaining a smooth curve, with the parameter α mediating the tradeoff. For instance, if α is zero, the smoothness constraint disappears and the minimizing curve will be a piecewise linear interpolant to the data; if α grows large, the smoothness constraint dominates and the curve approaches a simple linear fit to the data. For intermediate values of α, the minimizing curves balance the goodness-of-fit and smoothness constraints. It can in fact be shown that the minimizers of this functional will always be members of a class of functions known as natural cubic splines. These are piecewise cubic curves that join at the abscissa values ξ_i, where they are continuous up to and including the second derivative.

Clearly the choice of α determines the degree of smoothing that is applied to the data, and it is this parameter that is determined from the statistics of the data itself in an adaptive implementation of penalized least-squares smoothing using an algorithm known as generalized cross-validation [29]. Thus a generally different α is used in the smoothing of each of the M functions $P_k(\xi_i)$. The resulting continuous smoothed functions $P_k^s(\xi)$ must then be sampled to yield the discrete functions $P_k^s(\xi_i)$ which are subjected to the inverse DFT in step 3 above.

It should also be noted that while we have, for the sake of simplicity, discussed effective 2D smoothing, the technique can be extended to any number of dimensions. To smooth an n-dimensional function, one can simply take an $(n-1)$-dimensional Fourier transform of the function and then perform a set of 1D smoothings over the untransformed variable prior to taking an inverse $(n-1)$-dimensional Fourier transform [41].

In order to test the hypothesis that this effectively two-dimensional adaptive smoothing approach is superior to non-adaptive, one-dimensional smoothing such as the apodization used in filtered backprojection, we again calculated ideal-observer SNRs, this time for images reconstructed by FBP after various kinds of smoothing were applied to the conventional and dedicated SPECT projection data acquired for the geometry comparisons described in Section 2.1. As mentioned there, the aim here is to see which smoothing approach best preserves the SNR of the raw projection data. The detailed procedure is as follows:

1. The signal projections were scaled to simulate a desired tumor-background concentration ratio (6:1 in this case) and added to each of the 20 sets of background projections.

2. The slice through the center of the lesion was selected and the 20 corresponding signal-plus-background sinograms were reconstructed by filtered backprojection using ramp and Hanning filters with various cutoff frequencies (0.4, 0.6, 0.8, and 1.0 times the Nyquist frequency). The sinograms were also processed using the effective 2D smoothing procedure described above and reconstructed by filtered backprojection.

3. The 20 corresponding sinograms of background alone were processed in the same way.

4. An average signal image was determined by subtracting the average of the 20 background alone reconstructions from the average of the 20 signal-plus-background reconstructions. The signal power spectrum was computed by squaring the Fourier transform of this image.

5. While SPECT images are not stationary in general, the attenuated projections of a uniform cylinder of this diameter are quite flat over a broad central region, and thus one might reasonably expect the reconstructed images of this cylinder to be locally stationary near their center, precisely where the lesion is expected to lie [42]. The "local" Wiener spectrum in this region was computed from the 20 images of background alone by subtracting the average background image from each of the individual background images, resulting in 20 noise images. Each such image was multiplied by a circularly symmetric window of the form:

$$
w(\mathbf{r}) = \begin{cases} 1 & |\mathbf{r}| \leq 0.9R \\ \frac{1}{2}\left\{1 + \cos\left[\pi\left(|\mathbf{r}| - 0.9R\right)/0.2R\right]\right\} & 0.9R < |\mathbf{r}| < 1.1R \\ 0 & |\mathbf{r}| \geq 1.1R, \end{cases} \qquad (22)
$$

(with appropriate shifting for the off-center cylinder in the conventional geometry), where R is the radius of the circular region over which the noise is expected to be stationary (chosen to be 6 pixels) and $\mathbf{r}$ the radial position in the image. The power spectrum of each of the 20 images was computed by taking the square of the Fourier transform of the resulting image. The 20 power spectra were then averaged and scaled so that the volume under the Wiener spectrum equaled the average variance in the circle of radius R [43–45].

6. The ideal observer SNR was then determined by summing the quotient of the calculated signal spectrum and Wiener spectrum.

It should be noted that in using the ideal-observer framework at all it is implicitly being assumed that the data satisfy the assumptions discussed in Section 2.1: that the system is linear and that the noise in the planar or reconstructed images is additive, Gaussian, zero-mean, stationary, and independent of the presence or absence of the signal. Given the reasonably high count levels (~10-15/pixel) the fact that the signal is relatively small and low contrast, and the discussion of stationarity in point 5 above, the assumptions about the noise seem reasonable. The requirement of linearity seemingly undermines the use of the framework to analyze images that have been processed by adaptive, effective multi-dimensional smoothing. However, what is truly required for equation (1) to be meaningful is not linearity in the face of any possible input but more specifically that the system transfer function be the same whether the particular signal of interest is present or absent from the particular background of interest. Again, because the signal in question is relatively small and low contrast, it should not greatly affect the noise properties of the projection images and thus the effective multi-dimensional smoothing algorithm should yield a similar effective system transfer function whether or not the signal is present.

Having verified the performance of the smoothing when applied to sinograms containing a standard number of projection angles, we then tested it on few-view sinograms, after which periodic spline interpolation was used to generate additional views and FBP used to reconstruct. We acquired projections of a ventricular phantom filled with 3.27 mCi of Tc-99m. The phantom was not placed within a water-filled torso phantom. We imaged this phantom with a Picker PRISM 3000XP three-headed SPECT system fit with LEHRP collimators. We acquired SPECT studies containing 120 angular views over 360° of the phantom placed at five different radial offsets from the center of rotation: 0, 6, 9, 12, and 15 cm. We used a 25-cm radius circular orbit and step-and-shoot mode for all of the acquisitions; each head acquired to a 128x128 pixel image. A total of about 500,000 counts was collected. From this data we extracted sinograms corresponding to a single transverse slice and containing 15, 30, 60, and 120 views respectively. Thus we had 20 different sinograms, corresponding to the 20 possible combinations of radial offset and number of angular views. We reconstructed images from these 20 sinograms in 3 ways: (1) Simple reconstruction from the available views by conventional FBP using a Hanning filter

(cutoff=0.8). (2) Effective 2D adaptive smoothing of the sinogram and reconstruction from the available views by FBP using a ramp filter (cutoff=1.0). (3) Effective 2D adaptive smoothing of the sinogram, followed by spline interpolation from the available views to 120 views, and reconstruction by FBP using a ramp filter (cutoff=1.0).

2.4.3 Results and conclusions

The ideal-observer SNRs for the detection of a lesion with a 6:1 lesion-background concentration ratio are listed in Table 2 for the two different tomographic geometries and various kinds of smoothing. For reference, we also include the sinogram SNR values discussed in Section 2.1 above. The results indicate that

Smoothing Method	Conventional SPECT	Dedicated SPECT
Sinogram	6.7	10.7
Hanning (cutoff=0.4)	2.4	6.2
Hanning (cutoff=0.6)	3.1	8.0
Hanning (cutoff=0.8)	3.5	9.4
Hanning (cutoff=1.0)	3.7	9.9
Ramp (cutoff=0.4)	3.3	8.1
Ramp (cutoff=0.6)	3.7	9.7
Ramp (cutoff=0.8)	3.6	9.9
Ramp (cutoff=1.0)	3.7	9.3
Effectively 2D smoothing	5.5	10.6

Table 2: Ideal-observer SNRs for reconstructed conventional and dedicated SPECT images of a 6:1, 1-cm lesion using various kinds of smoothing.

effective two-dimensional smoothing provides improvement in SNR over other filtering approaches. Images corresponding to the two different geometries for selected processing methods are shown in Fig. 5.

For ease of comparison and simplicity of presentation of the cardiac phantom studies, we have grouped the reconstructed images by the number of angles in the original sinogram and we show in Fig. 6 the results for only three of the radial offsets: 0, 9, and 15 cm. We observe that reconstructions from available views without pre-smoothing or interpolation display star-shaped artifacts and a mottled appearance when the number of views is small. 2D smoothing alone reduces the noise visibility but has little effect on the star-shaped artifacts. Effectively 2D smoothing followed by interpolation to 120 views reduces both the appearance of noise and the star-shaped artifacts. However, when the radial offset is large and the number of initial views small, interpolation leads to prominent circular artifacts. By considering angular sampling requirements for objects of corresponding radial extent, it can be shown that these artifacts arise precisely when the initial angular sampling is insufficient. No processing can compensate for this sort of shortcoming in the data. However, when the sampling is adequate, the proposed technique allows FBP to produce high qual-
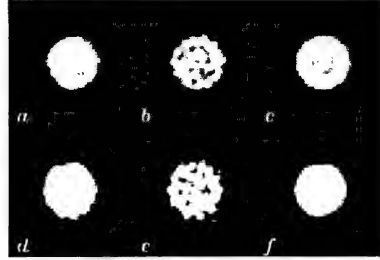
Figure 5: Reconstructed slices of a cylindrical phantom containing a 1-cm, 6:1 lesion for two different tomographic geometries. The top row corresponds to the dedicated SPECT geometry, the bottom row to conventional SPECT. The left column involves FBP reconstructions with a Hanning filter (cutoff=0.8), the middle column FBP reconstructions with a ramp filter (cutoff=0.6), and the right column FBP reconstructions after effectively 2D smoothing.

ity images from a small number of views. Indeed, we have conducted further studies with a cardiac phantom containing a lesion defect, and found that for a well-centered phantom, the proposed technique yields bullseye plots from as few as 15 or 30 angles that capture the defect as well as those obtained from 120 views.

2.5 Direct spline Radon inverse

2.5.1 Background

Most of the sinogram preprocessing approaches described so far have involved fitting of continuous smoothing and interpolating splines that were then resampled for input to the discrete FBP algorithm. There is an alternative approach, however, first proposed by Wahba [25] that allows reconstruction to proceed directly from the coefficients of the splines fit at each projection angle. We have simplified her approach, using relationships among spline coefficients to eliminate numerically unstable terms, and, perhaps most significantly, extended the approach to the three-dimensional Radon inversion problem, where it takes on a much simpler form than in two dimensions [46].

In the following, we will denote a distribution of activity in two dimensions by $f(x,y)$ and label each projection through it by the pair $\{\xi, \phi\}$, where ϕ specifies the *projection angle* and ξ the *projection distance*. The value of such a projection is given by the line integral of the distribution along the line specified by $\{\xi, \phi\}$ and will be denoted by $p(\xi, \phi)$. Similarly, we will denote a three-dimensional distribution by $f(x, y, z)$ and label each planar projection through it by the triplet $\{\xi, \theta, \phi\}$, where θ and ϕ specify the orientation of the plane and ξ the distance of the plane to the origin of the coordinates. The value of such a projection is given by the *planar* integral of the distribution over the plane specified by $\{\xi, \theta, \phi\}$ and will be denoted by $p(\xi, \theta, \phi)$. The functions $p(\xi, \phi)$ and
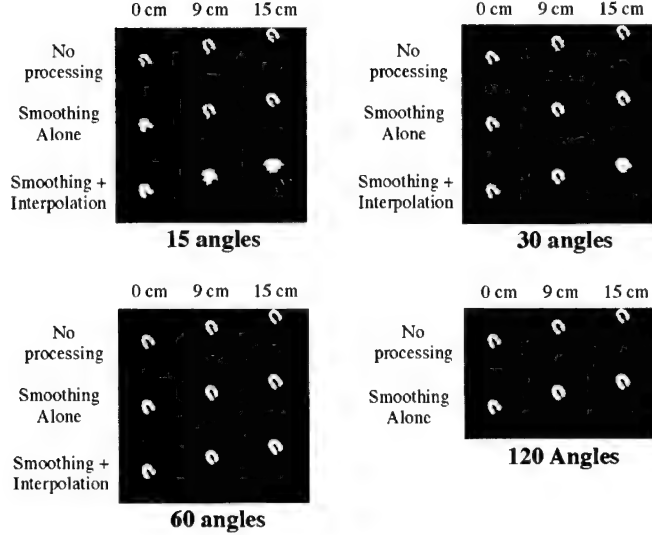
24

Figure 6: Images of a slice through a Data Spectrum ventricular phantom reconstructed by FBP after the indicated processing of the sinograms. The smoothing entailed the adaptive, effectively 2D smoothing described in the text, while interpolation was spline-based interpolation from the number of views listed to 120 views.

$p(\xi, \theta, \phi)$ are known as sinograms because in the two-dimensional case a point distribution in $\{x, y\}$ space maps to a sinusoid in $\{\xi, \phi\}$ space.

The Radon transform is a continuous, integral transform that relates the sinogram $p(\xi, \phi)$ to $f(x, y)$ in two dimensions and the sinogram $p(\xi, \theta, \phi)$ to $f(x, y, z)$ in three dimensions [29, 47, 48]. Inverting the Radon transform exactly to recover a distribution requires continuous, noise-free knowledge of the distribution's sinogram, which entails having an infinite set of perfect projection measurements. In practice, of course, one can only collect projection data in the two-dimensional case for a finite number of projection distances ξ_i (we call these discrete samples *projection bins*) at a finite number of projection angles ϕ_j, and the measurements are invariably contaminated with noise. In the three-dimensional case, the planar-integral projection data cannot generally be measured directly and must instead be generated from line-integral projection data; it is, however, still only generated for a finite number of projection bins ξ_i and projection angles ϕ_j and θ_k.

Because the sinogram $p(\xi, \phi)$ in two dimensions (or $p(\xi, \theta, \phi)$ in three dimensions) is known only on a finite grid of ξ_i and ϕ_j (or ξ_i, ϕ_j, and θ_k), we cannot invert the Radon transform exactly to recover the distribution $f(x, y)$ (or $f(x, y, z)$); we must instead turn to a discrete approximation of the inverse. For instance, one way of implementing the most popular two-dimensional Radon inversion algorithm—filtered backprojection (FBP) [49, 50]—begins with a dis-

25

crete filtration of the sinogram. The filtered samples of ξ_i for each projection angle ϕ_j are then backprojected onto the image grid and the resulting images summed to give a final reconstructed image. One way to view the backprojection step is to imagine casting a perpendicular ray from each image pixel to each projection angle in turn, summing the sinogram values picked up at each angle to obtain the final pixel value. In this view, the difficulty lies in determining what value to pick up from each projection angle, for in general the perpendicular line will not fall directly in the center of a projection bin. In the simplest schemes, one simply picks up the value of the bin the pixel projects onto, while in a more complicated approach one might perform a linear interpolation of the values in the two nearest projection bins. In the most sophisticated schemes, one uses a weighted average of the values in a slightly larger neighborhood. A similar procedure can be used to implement three-dimensional FBP [51].

The discreteness of the sinogram thus dictates discreteness in both the filtration and backprojection steps of the algorithm. If, however, one had a continuous, analytic expression for the sinogram at each projection angle—if the sinogram were a set of known one-dimensional functions of ξ—it might be possible to implement the filtration and backprojection steps in a continuous manner. The filtration could be performed analytically, and the resulting filtered projections would be continuous functions which, in the pixel-traversal view of backprojection described above, could be sampled wherever a projection might strike without any need to interpolate. Naturally, such an analytic, continuous expression for the sinogram cannot be obtained directly from any tomographic imaging system, but must rather be obtained by fitting an analytic expression to the discretely sampled data. Not every class of function that could be fit to the data would allow the filtration of the projections to be calculated in closed form, but Wahba [25] has shown that one class that does allow such a solution are the cubic splines, piecewise third-order polynomials that are continuous up to and including the second derivative at the connection points between pieces. This is the class of fitting functions we investigate in this paper, introducing Wahba's results (with some corrections and simplifications), and extending the treatment to the three-dimensional Radon transform. This method offers a certain conceptual appeal, as well as the advantage of directness when one wishes to smooth noisy projection data by fitting curves that minimize the popular penalized least-squares measure [35]. As it turns out, the minimizers of this measure are the natural cubic splines mentioned above and thus reconstruction can proceed directly from the coefficients of these splines in this case.

2.5.2 Methods

Inverse 2D Radon transform in coordinate space

The essential problem in two-dimensional tomography is the reconstruction of a distribution $f(x, y)$ (or $f(r, \theta)$ in polar coordinates) from knowledge of the discrete sinogram $p(\xi_i, \phi_j)$, where $i = -N, \ldots, N$ and $j = 1, \ldots, M$. This convention for the index i, particularly the choice of an odd number of projection

bins, will simplify the mathematical expressions to be derived below, but the proposed technique is applicable to geometries with an even number of bins as well. We assume in the present paper that we have a parallel-beam geometry.

Perhaps the most familiar way of expressing the inverse of the two-dimensional Radon transform is in terms of the frequency-space representation of the continuous sinogram:

$$f(r, \theta) = \int_0^\pi \int_{-\infty}^\infty |v| \, P(v, \phi) e^{j2\pi v\xi} \, dv \, d\phi, \tag{23}$$

where v is the spatial-frequency variable corresponding to ξ, $P(v, \phi)$ is the Fourier transform of the sinogram with respect to the variable ξ, and j is the imaginary number $\sqrt{-1}$. This expression provides the theoretical basis for FBP, as $|v|$ is just the familiar ramp filter. This expression may be written in coordinate space as

$$f(r, \theta) = \frac{1}{2\pi^2} \int_0^\pi J_{r,\theta}(\phi) d\phi, \tag{24}$$

where

$$J_{r,\theta}(\phi) = \left\{ \lim_{\epsilon \to 0} \left[\int_{-\infty}^{\xi' - \epsilon} \frac{p'(\xi, \phi)}{\xi' - \xi} d\xi + \int_{\xi' + \epsilon}^\infty \frac{p'(\xi, \phi)}{\xi' - \xi} d\xi \right] \right\}, \tag{25}$$

and in which $\xi' = r \cos(\theta - \phi)$ and $p'(\xi, \phi)$ is the first derivative of the sinogram $p(\xi, \phi)$ with respect to ξ [47, 52]. Taking the limit as $\epsilon \to 0$ of the sum of these two integrals allows us to avoid integrating over the singularity at $\xi' = \xi$. In general equations (24) and (25) are less useful than equation (23) because the data collected in PET, SPECT, or CT constitute samples of the sinogram itself, and do not provide any direct information about $p'(\xi, \phi)$. However, by fitting an analytic, differentiable function of ξ to the projection data at each angle, we could obtain an expression for $p'(\xi, \phi)$. If $p'(\xi, \phi)$ had an auspicious functional form, we would then be able to solve the integrals in equation (25) in closed form.

Interpolating and smoothing splines

To obtain an expression for the sinogram that is analytic and differentiable with respect to the variable ξ, we fit a function to the projection data at each angle. That is, for each angle ϕ_j, we fit a one-dimensional function of ξ, $\widehat{p}_{\phi_j}(\xi)$, to the sinogram values $p_{\phi_j}(\xi_i)$ measured on the $2N+1$ abscissas ξ_i ($i = -N, \ldots, N$). If the data is noiseless, it is desirable to use a function that passes through the points $p_{\phi_j}(\xi_i)$, which we call an *interpolating* curve, while if the data is noisy a *smoothing* curve may be more appropriate. One fitting framework that can handle both of these situations is known as penalized least-squares [35], in which the function $\widehat{p}_{\phi_j}(\xi)$ is chosen to be the minimizer of the functional

$$F\left[\widehat{p}_{\phi_j}(\xi)\right] = \sum_{i=-N}^N \left[p_{\phi_j}(\xi_i) - \widehat{p}_{\phi_j}(\xi_i) \right]^2 + \lambda \int_a^b \left(\widehat{p}_{\phi_j}''(\xi) \right)^2 d\xi, \tag{26}$$

27

where a and b are the endpoints of the interval on which the curve $\widehat{p}_{\phi_j}(\xi)$ is to be defined. The first term in equation (26) is the familiar squared-error measure, while the second is a measure of the smoothness of the fit curve. The parameter λ thus mediates the tradeoff between the competing goals of achieving a good fit to the data and maintaining a smooth curve. By choosing λ to be zero, we eliminate the smoothness constraint and ensure that the minimizing curve will be an interpolant to the data; if λ grows large, the smoothness constraint dominates and the curve approaches a linear fit to the data. For intermediate values of λ the minimizing curve balances the goodness-of-fit and smoothness constraints. The parameter λ can be chosen a priori [34] or it can be determined from the statistics of the data using an automatic procedure such as generalized cross-validation (GCV) [53].

The minimizers of this functional F belong to the class of functions known as natural cubic splines [34]. These are piecewise polynomial curves that join at the abscissa values ξ_i, where they are continuous up to and including the second derivative. They can be represented as

$$\widehat{p}_{\phi_j}(\xi) = a_i + b_i\xi + c_i\xi^2/2 + d_i\xi^3/3, \ \ \xi \in [\xi_i, \xi_{i+1}], \tag{27}$$

where a_i, b_i, c_i, and d_i are constants that fully specify the spline curve on the interval $[\xi_i, \xi_{i+1}]$. Of interest to the Radon inversion problem is the fact that we can approximate the first derivative of the sinogram for fixed angle ϕ_j by

$$p'(\xi, \phi_j) \cong \widehat{p}'(\xi) = b_i + c_i\xi + d_i\xi^2, \ \ \xi \in [\xi_i, \xi_{i+1}]. \tag{28}$$

Spline-based inverse of the 2D Radon transform

Given this analytic expression for the derivative of the sinogram, we can proceed with the inversion of the two-dimensional Radon transform in equation (24). While the sinogram now has a continuous representation in the variable ξ, it is still discrete in the angular variable. Assuming that the M angular samples are equally spaced over 180° or 360° (the result is the same in either case), the integral in equation (24) can be approximated by the sum

$$f(r, \theta) \cong \frac{1}{2\pi M} \sum_{j=1}^{M} J_{r,\theta}(\phi_j), \tag{29}$$

where $J_{r,\theta}(\phi_j)$ is given by equation (25). For a given coordinate (r, θ) in image space, and for a given projection angle ϕ_j, $\xi' = r\cos(\theta - \phi_j)$. We label the projection bin that ξ' falls in by m, that is, $\xi' \in [\xi_m, \xi_{m+1}]$. Using the expression for $p'(\xi, \phi)$ given by equation (28), $J_{r,\theta}(\phi_j)$ can be expressed as

$$J_{r,\theta}(\phi_j) = \sum_{i=-N, \, i\neq m-1,m,m+1}^{N-1} \int_{\xi_i}^{\xi_{i+1}} \frac{b_i + c_i\xi + d_i\xi^2}{\xi' - \xi} d\xi$$

28

$$+ \lim_{\epsilon \to 0} \left[\int_{\xi_m}^{\xi' - \epsilon} \frac{b_m + c_m \xi + d_m \xi^2}{\xi' - \xi} d\xi + \int_{\xi' + \epsilon}^{\xi_{m+1}} \frac{b_m + c_m \xi + d_m \xi^2}{\xi' - \xi} d\xi \right] \quad (30)$$

where the integrals of equation (25) are now expressed as sums of integrals over the subintervals between the original abscissa points, with appropriate accommodation for the singularity at ξ'. These integrals can be solved in closed form [25], and the resulting expression contains some potentially unstable terms. However, by combining these terms in a particular way and invoking spline identities, a stable form can be derived:

$$J_{r,\theta}(\phi_j) = T + \sum_{i=-N, \, i \neq m-1, m, m+1}^{N-1} (b_i + c_i \xi' + d_i \xi'^2) \ln \left(\frac{\xi' - \xi_i}{\xi' - \xi_{i+1}} \right)$$

$$- \sum_{i=-N}^{N-1} (c_i + 2 d_i \xi')(\xi_{i+1} - \xi_i) + \frac{1}{2} \sum_{i=-N}^{N-1} d_i \left[(\xi' - \xi_i)^2 - (\xi' - \xi_{i+1})^2 \right], \quad (31)$$

where T is given by

$$\begin{aligned}
T = & \left(b_{m-1} + c_{m-1} \xi' + d_{m-1} \xi'^2 \right) \ln \left(\xi' - \xi_{m-1} \right) \\
& + (d_m - d_{m-1})(\xi' - \xi_m)^2 \ln(\xi' - \xi_m) \\
& + (d_{m+1} - d_m)(\xi_{m+1} - \xi')^2 \ln(\xi_{m+1} - \xi') \\
& - \left(b_{m+1} + c_{m+1} \xi' + d_{m+1} \xi'^2 \right) \ln(\xi_{m+2} - \xi').
\end{aligned} \quad (32)$$

The 3D Radon transform in coordinate space

The essential problem in three-dimensional computed tomography is the reconstruction of a distribution $f(x, y, z)$ from knowledge of the discrete planar-integral sinogram $p(\xi_i, \theta_k, \phi_j)$, where $i = -N, \ldots, N$, $j = 1, \ldots, M_\phi$, and $k = 1, \ldots, M_\theta$ [54]. In general, these planar integrals are not measured directly by tomographic imaging systems, but must rather be calculated by "rebinning" the line integrals that are measured directly [51]. The inverse three-dimensional Radon transform has a form similar to the two-dimensional case, with a few differences that greatly simplify the task of evaluating it numerically. Specifically,

$$f(x, y, z) = \frac{1}{4\pi^2} \int_0^\pi \int_0^\pi p'' \left(\xi', \theta, \phi \right) \sin \theta d\phi d\theta, \quad (33)$$

where

$$\xi' = x \sin \theta \cos \phi + y \sin \theta \sin \phi + z \cos \theta, \quad (34)$$

and $p'' \left(\xi', \theta, \phi \right)$ is the second derivative of the three-dimensional sinogram with respect to ξ, evaluated at $\xi = \xi'$. This expression differs in two principal ways from the expression for the two-dimensional inverse Radon transform given by equations (24) and (25). First, it now involves the second derivative of the sinogram with respect to ξ rather than the first derivative and second, the convolution in ξ has disappeared. This reflects the fact that an inverse Radon

29

transform of odd degree can be calculated using purely local information—the value of the image at a point can be determined solely from information at points in the sinogram space that (x, y, z) projects onto, rather than from a convolution integral over all points in sinogram space as in the even-dimensional case [48,55].

Spline-based inverse of the 3D Radon transform

As in the two-dimensional case, we wish to fit an analytic function of ξ to each sequence of ξ_i labeled by a distinct pair $\{\phi_j, \theta_k\}$. We do so using the spline formalism described above and obtain

$$\widehat{p}_{\phi_j, \theta_k}(\xi) = a_i + b_i \xi + c_i \xi^2/2 + d_i \xi^3/3, \ \ \xi \in [\xi_i, \xi_{i+1}]. \tag{35}$$

Consequently the second derivative of the sinogram is approximately

$$p''(\xi, \theta_k, \phi_j) \cong \widehat{p}''_{\phi_j, \theta_k}(\xi) = c_i + 2d_i \xi, \ \ \xi \in [\xi_i, \xi_{i+1}]. \tag{36}$$

Now as in the two-dimensional case, the discreteness of the angular samples means that the two integrals give way to sums and we write

$$f(x, y, z) \cong -\frac{1}{4} \frac{1}{M_\theta} \frac{1}{M_\phi} \sum_{j=1}^{M_\phi} \sum_{k=1}^{M_\theta} J_{x,y,z}(\theta_k, \phi_j) \sin \theta_k, \tag{37}$$

where

$$J_{x,y,z}(\theta_k, \phi_j) = c_i + 2d_i \xi', \ \ \xi \in [\xi_i, \xi_{i+1}], \tag{38}$$

and

$$\xi' = x \sin \theta_k \cos \phi_j + y \sin \theta_k \sin \phi_j + z \cos \theta_k.$$

The simplicity of the three-dimensional inversion is now apparent, for the functions J can be evaluated in a straightforward manner whereas in the two-dimensional case evaluation of the functions J involved performing a complicated integral over ξ and taking care in handling numerically unstable terms.

Application to phantom and real data

In order to demonstrate that the 2D direct-spline inverse of the Radon transform produces images of comparable or superior quality to filtered backprojection (FBP), we reconstructed images of a numerical Hoffman brain phantom [56] using both methods. The sinogram consisted of 128 simulated noiseless projections of the phantom, taken over 360° and each comprising 400 projection bins. The sinogram contained a total of 1.72×10^8 counts. We first reconstructed the phantom using standard area-weighted FBP with a ramp filter (cutoff=1.0 times the Nyquist frequency). We then fit an interpolating spline to the data at each of the 128 projection angles and used the 2D direct-spline technique to reconstruct. Poisson noise was then added to the sinogram. Images were

reconstructed using FBP with a ramp filter (cutoff=1.0) as well as the direct-spline technique using an interpolating spline in order to see how the algorithms compared in the presence of noise without prior smoothing. Smoothing splines were then fit to the projection data at each angle, using GCV to determine the smoothing parameter, and an image reconstructed from the coefficients using the direct-spline method. In order to examine the performance of FBP in the face of data with the same degree of smoothness, we sampled these smoothing splines to generate a discrete sinogram that was reconstructed using FBP with a ramp filter (cutoff=1.0).

For the 3D case, we reconstructed images of a Data Spectrum ventricular phantom from projection data acquired on a Picker XP3000 three-headed SPECT system fitted with high-resolution, parallel-hole collimators. The phantom was filled with 3.27 mCi of Tc-99m and placed at the center of rotation. Each head collected data on a 128x128 grid and at 120 projection angles over 360°. We rebinned the projection data from a single head to generate planar integrals on a 128x60x120 grid. Images were reconstructed from this planar-integral data using 3D FBP, and also using the 3D direct-spline inversion method after splines were fit to the data as described above. We then fit smoothing splines to the planar-integral data and reconstructed directly from the spline coefficients. Finally, we sampled the smoothing splines to generate a smoothed, discrete sinogram and used that as input to the 3D FBP algorithm.

Resolution, noise, and signal-to-noise studies

In order to compare quantitatively the resolutions of the direct-spline algorithms (both two- and three-dimensional) with their FBP counterparts, we acquired projection images of a small (1-cm) spherical lesion containing 7.6 mCi of Tc-99m placed in an 800 cc cylindrical phantom containing cold (zero-activity) water. A Picker XP2000 two-headed SPECT system fitted with ultra-high-resolution, parallel-hole collimators was used. The heads rotated at their minimum radius of rotation (9 cm) and acquired 120 views over 360° onto a 128x128 matrix (pixel size=4.67 mm).

For the two-dimensional algorithms, we extracted the 2D sinogram corresponding to the slice through the center of the lesion and reconstructed images using FBP with a ramp filter (cutoff=1.0) as well as using the direct spline inversion with interpolating splines. The reconstructed lesion was approximately a symmetric 2D Gaussian in shape and we determined its full-width half-maximum by collapsing it into a one-dimensional function and fitting this profile with a Gaussian curve. For the three-dimensional reconstruction algorithms, we rebinned the projection data to generate planar-integral data on a 128x60x120 grid. We then used 3D FBP and the 3D direct spline method (using interpolating splines) to reconstruct the slice through the center of the lesion and determined the FWHM of the resulting Gaussian by the same method as above.

In order to isolate the contribution of the reconstruction algorithm to the FWHM of the lesion in the reconstructed images, the contribution from the

lesion's inherent width as well as the imaging system's point-spread function had to be removed. The net effect of these two factors was estimated by determining the average FWHM of the lesion as it appeared in the 120 projection images. Assuming then that the reconstruction algorithms could be characterized by Gaussian point-spread functions, the FWHM of these functions were determined by subtracting (in quadrature) the average projection FWHM from the FWHMs of the reconstructed lesions discussed above.

To characterize the noise level in images reconstructed by the direct-spline methods and their FBP counterparts, we acquired 20 1-minute projection data sets of the same 800 cc cylindrical phantom used in the resolution studies above, this time containing 3.7 mCi of Tc-99m and no lesion. One slice of this uniform cylinder was reconstructed for each of the 20 datasets using 2D FBP, 3D FBP, 2D spline inversion, and 3D spline inversion (both of these using interpolating splines). For a given algorithm, the same six circular regions of interest (ROI) were examined in each of the 20 slices and the coefficient of variation (the standard deviation of the pixel values in the ROI divided by the mean of the pixel values in the ROI) calculated for each of the 120 ROIs. The average of these 120 coefficients of variation was then computed.

It is not uncommon for a reconstruction algorithm to offer enhanced resolution at the price of amplified noise. The overall effect of such a tradeoff is sometimes better characterized by computing a signal-to-noise ratio (SNR). We used the two datasets described above to compute the ideal-observer SNR using the method described in section 2.4.2.

2.5.3 Results and conclusions

The results of reconstructing the Hoffman brain phantom with and without noise using both the 2D direct-spline inverse and 2D FBP are depicted in Fig. 7. The algorithms clearly yield qualitatively similar results. The results of reconstructing the ventricular phantom data using 3D direct-spline inversion with interpolating splines, 3D FBP, 3D direct-spline inversion with smoothing splines, and 3D FBP using a sinogram resampled from the smoothing splines are depicted in Fig. 8. The algorithms are again seen to yield qualitatively similar results.

The resolution measurements for the four basic algorithms—2D direct-spline inversion, 2D FBP with a ramp filter (cutoff=1.0), 3D direct-spline inversion, and 3D FBP—are summarized in Table 3. The results indicate that the direct-

Algorithm	FWHM
2D direct spline	1.6 mm
2D FBP	4.5 mm
3D direct spline	3.9 mm
3D FBP	5.0 mm

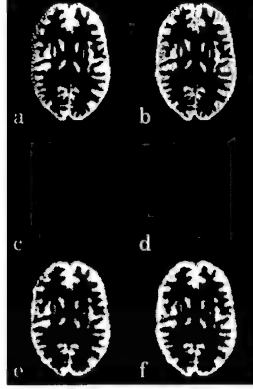Table 3: FWHM of in-plane reconstruction point-spread functions

Figure 7: Reconstructions of a Hoffman brain phantom from simulated projections without noise (a-b) and with Poisson noise added (c-f). Reconstruction methods are: (a) FBP with ramp filter (cutoff=1.0), (b) direct-spline inversion using interpolating splines, (c) FBP with ramp filter (cutoff=1.0), (d) direct-spline inversion using interpolating splines, (e) FBP from a sinogram generated by sampling smoothing splines, (f) direct-spline inversion using smoothing splines.

spline inversions have superior resolution to FBP in both the 2D and 3D cases and also that the 2D algorithms have superior resolution to the 3D algorithms.

The results of the noise study are summarized in Table 4, where it can be

Algorithm	COV
2D direct spline	0.60
2D FBP	0.39
3D direct spline	0.34
3D FBP	0.23

Table 4: Coefficients of variation for various reconstruction algorithms

seen that the noise level in the direct-spline reconstructions is higher than that in the FBP reconstructions and that the noise level in the 2D reconstructions is higher than that in the 3D reconstructions.

Finally, the ideal-observer signal-to-noise ratio results are summarized in Table 5 for the four basic algorithms as well as their counterparts using smoothing splines. We observe that the direct-spline algorithms have slightly lower SNRs than their FBP counterparts when using interpolating splines, while the SNRs become comparable when using smoothing splines. Furthermore, the use of smoothing splines seems to have little effect on SNR in the 2D case while degrading it in the 3D case. All of the reconstructed images are seen to have lower SNRs than the raw projection data, a fact that is discussed in greater detail in the next section. Typical images reconstructed using each of these
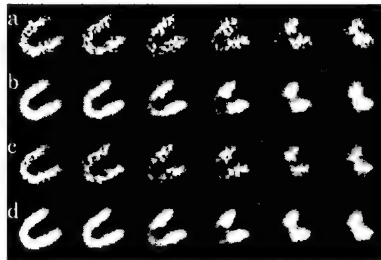
Figure 8: Selected slices of a ventricular phantom reconstructed by (a) 3D direct-spline inversion using interpolating splines, (b) 3D direct-spline inversion using smoothing splines, (c) 3D FBP, and (d) 3D FBP from a sinogram obtained by sampling the smoothing splines in (b).

Algorithm	Ideal-observer SNR
Sinogram	10.7
2D interpolating spline	7.9
2D FBP	8.6
2D smoothing spline	8.4
2D FBP w/ smth. spline	8.4
3D interpolating spline	9.0
3D FBP	9.6
3D smoothing spline	7.5
3D FBP w/ smth. spline	7.0

Table 5: Ideal-observer SNRs for various reconstruction algorithms

eight methods are shown in Fig. 9.

As discussed in section 2.5.1, the principal difference between the 2D and 3D direct-spline inversion algorithms and FBP is in the nature of the interpolation step upon backprojection. The interpolation in FBP is simply less accurate than the more sophisticated cubic-spline interpolation used in the direct-spline method. The cruder FBP interpolation is more likely to smooth over high-frequency variations in the projection data than is cubic-spline interpolation, and thus it is not surprising that the FBP algorithms have inferior resolution to the spline-based algorithms, as illustrated in Table 3. However, because the high-frequency components of the data include considerable noise as well, the FBP algorithms would be expected to produce less noisy reconstructions than the spline-based reconstructions. This expectation is confirmed by the results of the noise study reported in Table 4.

The 3D direct-spline and FBP algorithms are both seen to have inferior resolution and lower noise levels than their 2D counterparts. This can be attributed to the fact that the 3D reconstruction process involves an additional averaging or smoothing step which occurs when the raw projection data is rebinned into a planar-integral sinogram by performing area-weighted forward projections of
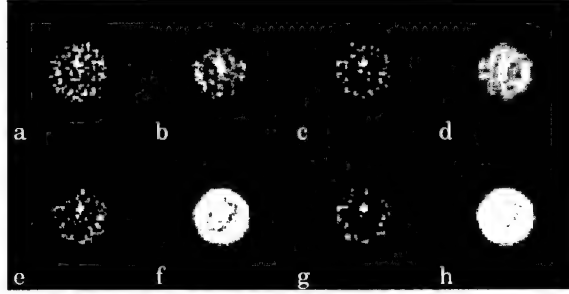
34

Figure 9: Reconstructions of a selected slice of a cylindrical phantom containing a spherical lesion. Reconstruction methods: (a) 2D direct-spline inversion using interpolating splines, (b) 2D direct-spline inversion using smoothing splines, (c) 2D FBP, (d) 2D FBP from a sinogram obtained by sampling the smoothing splines in (b), (e) 3D direct-spline inversion using interpolating splines, (f) 3D FBP, (g) 3D direct-spline inversion using smoothing splines, (h) 3D FBP from a sinogram obtained by sampling the smoothing splines in (g)

the 2D projection data at each projection angle.

Table 5 lists the ideal-observer SNR for the raw projection data and for the various reconstruction approaches. It is a fact that processing or even image reconstruction can never improve the ideal-observer SNR over that found in the raw projection data. However, these operations can certainly diminish the SNR if they are in some way singular and if the signal vector has components in the null space. We observe that all the reconstructed image SNRs are in fact lower than that of the raw projection data. The differences among those reconstructed image SNRs give some clue as to how much of the information contained in those projections is preserved in the reconstructed image. For instance, we see that ideal-observer SNRs are slightly lower for the 2D and 3D direct-spline inversions using interpolating splines than for their FBP counterparts using ramp filters. For this particular detection task, then, the interpolating-spline algorithm's amplification of noise outweighs the improvement it affords in resolution relative to FBP. However, when the noise is mitigated prior to reconstruction, as when the projection data has been fitted with smoothing splines, the SNR gap between the spline algorithms and FBP is considerably narrowed in the 2D case and reversed in the 3D case. This suggests that the spline-based algorithms may be of greatest use when resolution is paramount and the data contains relatively little noise, a situation more often encountered in computed tomography than in nuclear medicine. The use of smoothing splines is seen to provide little or no improvement in SNR in the 2D case. Smoothing does affect the ideal-observer SNRs in the 3D case, but for the worse. It is clear from examining the images of Fig. 9 that the reconstructed images using 3D algorithms and smoothing splines have an oversmoothed appearance. This can most likely be attributed to the fact, mentioned above, that the 3D reconstruction process effectively involves a prior smoothing during the rebinning step. The adaptive smoothing

algorithm certainly makes allowances for the lower variability in the rebinned data and smooths this data less than it would the raw projection data. However, the modified statistics of the rebinned data simply do not agree as well with the statistical model assumed by the smoothing algorithm, so it is perhaps not surprising that it yields a sub-optimal result. It remains a topic for further investigation as to whether smoothing the raw projection data prior to the rebinning step produces a better result.

3 Conclusions

The work of the past year has touched on a wide variety of topics related to the reconstruction of dedicated SPECT scintimammographic images from a smaller number of views than is usually used in nuclear medicine tomography. The following principal conclusions have emerged from the work:

1. An ideal-observer SNR analysis of the data obtained in planar, conventional SPECT, and dedicated SPECT scintimammography indicated that the dedicated SPECT geometry is the best of the three for detecting typical malignant breast lesions given equal total imaging time for all the modalities. This finding reaffirms the assumption underlying this project: that despite the fact that no one has yet developed a dedicated SPECT sctintimammographic system, its obvious advantages make it almost inevitable that it will win a role in the diagnosis and management of breast cancer.

2. Further application of the ideal-observer framework to study the dependence of dedicated SPECT scintimammography SNR on the number of projection views acquired revealed an approximate square root relationship. This implies, for instance, that cutting in half the number of projection views acquired only results in a $\sqrt{2}$ reduction in the SNR.

3. Images of a numerical breast phantom reconstructed by an unregularized ART algorithm were found to be clearly inferior to those reconstructed by ramp-filtered FBP, and especially so in the presence of noise. Moreover, even in the case of a few-view reconstruction, the lesions were more detectable in the FBP reconstruction, despite prominent star artifacts, than they were in the ART reconstruction. This finding had three consequences for the research. First, it dissuaded us from pursuing the implementation of a binary version of the ART algorithm until adequate regularization approaches have been explored. Second, it impelled us to begin exploring such regularization approaches as well as the related statistical image reconstruction approaches. Third, it inspired us to reexamine FBP and to explore combinations of smoothing and interpolation algorithms for sinogram preprocessing in the hopes of eliminating the star artifact common in few-view FBP.

36

4. The first conclusion to emerge from our study of interpolation methods was the mathematical equivalence of zero-padding and circular-sampling theorem interpolation and the little-appreciated fact that zero-padding is exact and equivalent to Whittaker-Shannon interpolation when interpolating a periodic, bandlimited function from a set of samples satisfying the Nyquist condition. This equivalance allowed us to omit CST interpolation from the set of those being considered for use in sinogram interpolation, as zero-padding has much more favorable computational properties.

5. Studies of the noise properties of interpolation methods yielded three interesting conclusions. The first is that when interpolating from samples corrupted by white noise, CST and ZP yield interpolated points with constant variance. The second is that when the number N of initial samples is odd, this constant variance equals the variance in the measured samples, while when the number of initial samples is even it equals $(N-1)/N$ times the variance in the measured samples. This indicates that there is a slight advantage to using an even number of samples, at least when N is small. The third is that periodic spline interpolation yields nonconstant variance in the interpolated points: equal to the initial variance at points coincident with measured points and falling to a minimum between such points. This suggests that periodic spline interpolation has a slight variance-reducing advantage over ZP interpolation.

6. Studies of the empirical accuracy of various types of periodic interpolation approaches using statistical hypothesis testing lead to the conclusion that periodic spline interpolation is superior to linear or zero-padding interpolation in the face of typical tomographic data. This finding, coupled with the variance-reduction property discussed in point 5 indicate that periodic spline interpolation is the best choice for interpolation of additional angular views in tomography.

7. We developed an effectively two-dimensional, adaptive smoothing approach that exploits Fourier transforms to reduce the dimensionality of the smoothing problem and we used ideal-observer analysis to show that use of this approach prior to reconstruction by FBP preserves more of the information content of the sinogram than the use of spatially invariant apodization filters. The technique was then applied to few-view data and then followed by interpolation of additional views with promising results.

8. Finally, we examined and tested a direct spline-based Radon inversion technique that minimizes the inaccuracies introduced by the usual discretization of the image reconstruction process. While computationally intensive in two dimensions, the technique is quite straightforward in the three-dimensional case. In both cases it was found to yield higher resolution, albeit noisier images than FBP, with slightly reduced SNRs. It remains to be seen whether it enhances human observer performance.

References

[1] American Cancer Society, "Cancer facts and figures," Atlanta, 1996.

[2] I. Andersson, "Mammographic screening and mortality from breast cancer: Malmö mammographic screening trial," *Br. J. Med.*, vol. 297, pp. 943–948, 1988.

[3] J. Frisell, G. Eklund, L. Hellström, E. Lidbrink, L. Rutqvist, and A. Somell, "Randomized study of mammographic screening—preliminary report on mortality in the Stockholm trial," *Breast Cancer Res. and Treat.*, vol. 18, pp. 49–56, 1991.

[4] A. B. Miller, C. J. Baines, T. To, and C. Wall, "Canadian national breast screening study," *Can. Med. Assoc. J.*, vol. 147, pp. 1459–1476, 1992.

[5] D. B. Kopans, "The positive predictive value of mammography," *AJR*, vol. 158, pp. 521–526, 1992.

[6] E. Bombardieri, F. Crippa, L. Maffioli, and M. Greco, "Nuclear medicine techniques for the study of breast cancer," *Eur. J. Nucl. Med.*, vol. 24, pp. 809–824, 1997.

[7] A. D. Waxman, "The role of Tc-99m Methoxyisobutylisonitrile in imaging breast cancer," *Seminars in Nuclear Medicine*, vol. 27, pp. 40–54, 1997.

[8] C. H. Kao, S. J. Wang, and T. J. Liu, "The use of technetium-99m methoxy-isobutylisonitrile breast scintigraphy to evaluate palpable breast masses," *Eur. J. Nucl. Med.*, vol. 21, pp. 432–436, 1994.

[9] I. Khalkhali, J. Cutrone, I. Mena, L. Diggles, R. Venegas, H. Vargas, B. Jackson, and S. Klein, "Technetium-99m-sestamibi scintimammography of breast lesions: Clinical and pathological follow-up," *J. Nucl. Med.*, vol. 36, pp. 1784–1789, 1995.

[10] I. Khalkhali, I. Mena, and L. Diggles, "Review of imaging techniques for the diagnosis of breast cancer: A new role of prone scintimammography using technetium-99m-sestamibi," *Eur. J. Nucl. Med.*, vol. 21, pp. 357–362, 1994.

[11] I. Khalkhali, J. Cutrone, I. Mena, L. Diggles, R. Venegas, H. Vargas, B. Jackson, S. Khalkhali, J. Moss, and S. Klein, "Scintimammography: The complementary role of Tc-99m sestamibi prone breast imaging for the diagnosis of breast carcinoma," *Radiology*, vol. 196, pp. 421–426, 1995.

[12] J. Villanueva-Meyer, M. H. Leonard Jr., E. Briscoe, F. Cesani, S. A. Ali, S. Rhoden, M. Hove, and D. Cowan, "Mammoscintigraphy with technetium-99m-sestamibi in suspected breast cancer," *J. Nucl. Med.*, vol. 37, pp. 926–930, 1996.

[13] R. Taillefer, A. Robidoux, R. Lambert, S. Turpin, and J. Laperrière, "Technetium-99m-sestamibi prone scintimammography to detect primary breast cancer and axillary lymph node involvement," *J. Nucl. Med.*, vol. 36, pp. 1758–1765, 1995.

[14] H. Palmedo, A. Schomburg, F. Grünwald, P. Mallman, D. Krebs, and H.-J. Biersack, "Technetium-99m-MIBI scintimammography for suspicious breast lesions," *J. Nucl. Med.*, vol. 37, pp. 626–630, 1996.

[15] H. Palmedo, F. Grünwald, H. Bender, A. Schomburg, P. Mallmann, D. Krebs, and H.-J. Biersack, "Scintimammography with technetium-99m methoxyisobutylisonitrile: Comparison with mammography and magnetic resonance imaging," *Eur. J. Nucl. Med.*, vol. 23, pp. 940–946, 1996.

[16] F. Scopinaro, M. Ierardi, L. Porfiri, N. Tiberio, G. De Vincentis, S. Mezi, P. Cannas, T. Gigliotti, and L. Marzetti, "Tc-99m-MIBI prone scintimammography in patients with high and intermediate risk mammography," *Anticancer Research*, vol. 17, pp. 1635–1638, 1997.

[17] F. Scopinaro, O. Schillaci, W. Ussof, K. Nordling, R. Capoferro, G. De Vincentis, R. Danieli, M. Ierardi, V. Picardi, R. Tavolaro, and A. C. Colella, "A three-center study on the diagnostic accuracy of 99mtc-mibi scintimammography," *Anticancer Research*, vol. 17, pp. 1631–1634, 1997.

[18] A. Maurier, D. F. Caroline, F. J. Jadali, T. A. Manzone, W. P. Maier, F. C. Au, and S. F. Schnall, "Limitations of craniocaudal thallium-201 and technetium-99m-sestamibi mammoscintigraphy," *J. Nucl. Med.*, vol. 36, pp. 1696–1700, 1995.

[19] J. Maublant, M. de Latour, D. Mestas, A. Clemenson, S. Charrier, V. Feillel, G. Le Bouedec, P. Kaufmann, J. Dauplat, and A. Veyre, "Technetium-99m-sestamibi uptake in breast tumor and associated lymph nodes," *J. Nucl. Med.*, vol. 37, pp. 922–925, 1996.

[20] L. Diggles, I. Mena, and I. Khalkhali, "Technical aspects of prone dependent-breast scintimammography," *J. Nucl. Med. Tech.*, vol. 22, pp. 165–170, 1994.

[21] M. A. Nathan, J. E. Seabold, T. Barloon, J. Quesenberry, D. L. Bushnell, R. A. Robinson, and D. C. Young, "Planar vs. SPECT Tc-99m MIBI evaluation of suspicious breast lesions on mammography: Histologic correlation," *J. Nucl. Med.*, vol. 35, p. 229P, 1994.

[22] N. Nagaraj, A. Waxman, G. Ashok, S. Khan, L. Memsic, J. Yadegar, and E. Phillips, "Comparison of SPECT and planar Tc-99m sestamibi (MIBI) imaging in patients with carcinoma of the breast," *J. Nucl. Med.*, vol. 35, p. 299P, 1994.

[23] R. Tiling, M. Pechmann, H. Sommer, R. Moser, K. Tatsch, and K. Khan, "Does SPECT improve the diagnostic accuracy of planar scintimammography with sestamibi?," *J. Nucl. Med.*, vol. 37, p. 252P, 1996.

[24] H. Wang, C. Scarfone, K. L. Greer, R. E. Coleman, and R. J. Jaszczak, "Prone breast tumor imaging using vertical axis-of-rotation SPECT systems: An initial study," *IEEE Trans. Nucl. Sci.*, vol. 44, pp. 1271–1276, 1997.

[25] G. Wahba, "A new approach to the numerical evaluation of the inverse Radon transform with discrete, noisy data," Tech. Rep. MT-479, Technion Preprint Series, 1980.

[26] P. J. La Rivière, X. Pan, and B. C. Penney, "Ideal-observer analysis of lesion detectability in planar, conventional SPECT, and dedicated SPECT scintimammography using effective multi-dimensional smoothing," *IEEE Trans. Nucl. Sci.*, vol. 45, pp. 1273–1279, 1998.

[27] International Comission on Radiation Units and Measurements, "Medical imaging: The assessment of image quality," 7910 Woodmont Ave., Bethesda, MD, 20814, 1996.

[28] J. Yao and H. H. Barrett, "Predicting human performance by a channelized Hotelling observer model," in *Proc. SPIE*, vol. 1768, pp. 161–168, 1992.

[29] G. T. Herman, *Image Reconstruction from Projections: The Fundamentals of Computerized Tomography.* Boston: Academic Press, 1980.

[30] R. L. Siddon, "Fast calculation of the exact radiological path for a three-dimensional CT array," *Med. Phys.*, vol. 12, pp. 252–255, 1985.

[31] R. W. Schafer and L. R. Rabiner, "A digital signal processing approach to interpolation," *Proc. IEEE*, vol. 61, pp. 692–702, 1973.

[32] K. P. Prasad and P. Satyanarayana, "Fast interpolation algorithm using FFT," *Electron. Lett.*, vol. 22, pp. 185–187, 1986.

[33] D. Fraser, "Interpolation by the FFT revisited—an experimental investigation," *IEEE Trans. Acoust., Speech, Signal Processing*, vol. 37, pp. 665–675, 1989.

[34] J. A. Fessler, "Tomographic reconstruction using information-weighted spline smoothing," in *Information Processing in Medical Imaging* (H. H. Barrett and A. F. Gmitro, eds.), pp. 290–300, Berlin: Springer-Verlag, 1993.

[35] P. J. Green and B. W. Silverman, *Nonparametric Regression and Generalized Linear Models.* London: Chapman Hall, 1994.

[36] P. J. La Rivière and X. Pan, "Mathematical equivalence of zero-padding and circular sampling thorem interpolation with implications for direct Fourier image reconstruction," in *Proc. SPIE*, vol. 3338, pp. 1117–1126, 1998.

[37] E. O. Brigham, *The Fast Fourier Transform and Its Applications*. Englewood Cliffs: Prentice Hall, 1988.

[38] H. Stark, "Sampling theorems in polar coordinates," *J. Opt. Soc. Am.*, vol. 69, pp. 1519–1525, 1979.

[39] T. J. Cavicchi, "DFT time-domain interpolation," *IEE Proceedings-F*, vol. 139, pp. 207–211, 1992.

[40] A. Williams and K. Burrage, "Surface fitting using GCV smoothing splines on supercomputers," in *CD-ROM Proceedings of the 1995 ACM/IEEE Conference on Supercomputing*, 1995.

[41] X. Pan, "A general approach for multidimensional smoothing," *Med. Phys.*, vol. 25, pp. 562–570, 1998.

[42] S. C. Moore, M. F. Kijewski, S. P. Müller, and B. L. Holman, "SPECT image noise power: Effects of nonstationary projection noise and attenuation compensation," *J. Nucl. Med.*, vol. 29, pp. 1704–1709, 1988.

[43] S. J. Riederer, N. J. Pelc, and D. A. Chesler, "The noise power spectrum in computed x-ray tomography," *Phys. Med. Biol.*, vol. 23, pp. 446–454, 1978.

[44] K. Hanson, "Detectability in computed tomographic images," *Med. Phys.*, vol. 6, pp. 441–451, 1979.

[45] M. F. Kijewski and P. F. Judy, "The noise power spectrum of CT images," *Phys. Med. Biol.*, vol. 32, pp. 565–575, 1987.

[46] P. J. La Rivière and X. Pan, "Spline-based inverse radon transform in two and three dimensions," *IEEE Trans. Nucl. Sci.*, vol. 45, 1998. In press.

[47] H. H. Barrett, "The Radon transform and its applications," in *Progress in Optics XXI* (E. Wolf, ed.), pp. 217–286, Amsterdam: Elsevier Science Publishers, 1984.

[48] S. Deans, *The Radon Transform and Some of Its Applications*. New York: Wiley, 1983.

[49] L. A. Shepp and B. F. Logan, "The Fourier reconstruction of a head section," *IEEE Trans. Nucl. Sci.*, vol. 21, pp. 21–43, 1974.

[50] R. H. Huesman, G. T. Gullberg, W. L. Greenberg, and T. F. Budinger, *User Manual, Donner Algorithms for Reconstruction Tomography*. Lawrence Berkeley Laboratory, University of California, 1977.

[51] C. W. Wu, *Fully Three-Dimensional Reconstruction in PET and SPECT by the Use of Three-Dimensional Radon Transforms.* PhD thesis, The University of Chicago, 1994.

[52] G. T. Herman and A. Naparstek, "Fast image reconstruction based on a Radon inversion formula appropriate for rapidly collected data," *SIAM J. Applied Mathematics*, vol. 33, pp. 511–533, 1977.

[53] D. M. Bates, M. Lindstrom, G. Wahba, and B. Yandell, "GCVPACK routines for generalized cross validation," *Commun. Statist. Simul. Comput.*, vol. 16, pp. 263–297, 1987.

[54] M. Y. Chiu, H. H. Barrett, and R. G. Simpson, "Three-dimensional image reconstruction from projections," *J. Opt. Soc. Am.*, vol. 70, pp. 755–762, 1980.

[55] F. Natterer, *The Mathematics of Computerized Tomography.* Stuttgart: Wiley, 1986.

[56] E. J. Hoffman, P. D. Cutler, W. M. Digby, and J. C. Mazziotta, "3-D phantom to simulate cerebral blood flow and metabolic images for PET," *IEEE Trans. Nucl. Sci.*, vol. 37, pp. 616–620, 1990.